Petroleum Science 20 (2023) 60–86

Contents lists available at ScienceDirect

Petroleum Science

journal homepage: www.keaipublishing.com/en/journals/petroleum-science

Original Paper

Organic matter pores in the chang 7 lacustrine shales from the Ordos Basin and its effect on reflectance measurement

Peng Pang [a], Hui Han [a, b, c, *], Xiu-Cheng Tan [a], Shi-Meng Ren [d], Chen Guo [a], Lin Xie [a], Ling-Li Zheng [e], Hai-Hua Zhu [a], Yuan Gao [f], Yun-Hui Xie [g]

[a] School of Geoscience and Technology, Southwest Petroleum University, Chengdu, Sichuan, 610500, China
[b] Natural Gas Geology Key Laboratory of Sichuan Province, Southwest Petroleum University, Chengdu, Sichuan, 610500, China
[c] Shale Gas Industry Development Institute of Sichuan Province, Chengdu, Sichuan, 610500, China
[d] The First Branch Mud Logging Company, CNPC Bohai Drilling Engineering Co. Ltd., Tianjin, 300457, China
[e] State Key Laboratory of Oil and Gas Reservoir Geology and Exploration, Southwest Petroleum University, Chengdu, Sichuan, 610500, China
[f] Beijing Center for Physical and Chemical Analysis, Beijing, 100089, China
[g] Nursing College, Guizhou University of Traditional Chinese Medicine, Guiyang, Guizhou, 520002, China

ARTICLE INFO

Article history:
Received 3 April 2022
Received in revised form
28 May 2022
Accepted 25 August 2022
Available online 30 August 2022

Edited by Jie Hao and Teng Zhu

Keywords:
Ordos Basin
Chang 7 member
OM pore
Macerals
Differential developmental characteristics
Reflectance

ABSTRACT

To quantify the pore characteristics of various macerals in Chang 7 lacustrine shales, macerals were effectively identified according to their optical and morphological characteristics, and the nanoscale pore structure of macerals was observed by scanning electron microscope. Meanwhile, the reflectances of different positions in the same pieces of vitrinite or solid bitumen with heterogeneous pores development were measured. The results showed that the average contents of sapropelinite, liptinite, vitrinite, inertinite and solid bitumen are 42.7%, 8.7%, 13.6%, 13.8% and 21.2%, respectively, which suggests that the source of the organic matter of the Chang 7 shales is a mixed source input. The organic pores of Chang 7 shales are enriched, and the pore shapes are mostly round or elliptical. The pore size of organic pores has a wide distribution, mainly concentrate in the range of 100–400 nm, and the average plane porosity of organic pores is 10.13%. The size order of the organic pores in various macerals is: solid bitumen < bituminite < alginite < vitrinite < fusinite < liptinite. The abundance order of organic matter pores of each maceral is as follows: alginite > fusinite > bituminite > solid bitumen > vitrinite > liptinite. OM pores are mainly contributed by bituminite, solid bitumen and fusinite. The plane porosity of bituminite increases with maturity. In the process of thermal evolution, the plane porosity of fusinite is distributed in the two ranges of 20%–28% and 1%–7%. The former is mainly the primary pores of the fusinite itself, and the latter is the secondary pores formed in the thermal evolution. As for the organic pores of other macerals, no obvious thermal evolution law was found. Meanwhile, the surface imperfections of vitrinite or solid bitumen is enhanced by the enrichment of organic pores (an increase in pore size or pore number), which may result in the underestimation of their reflectances.

1. Introduction

Shale oil and shale gas are unconventional resources with great development potential and are gradually being produced commercially by various countries (Han et al., 2019; Cao et al., 2020a; Pang et al., 2021). Shale pores as the main storing space for shale gas and oil have been studied extensively (Curtis, 2002; Slatt and O'Brien, 2011; Ma et al., 2015; Wang et al., 2015a, b; Guo et al., 2018; Han et al., 2020), which can be divided into organic matter (OM) pores, interparticle pores and intraparticle pores (Loucks et al., 2012). OM pores refer to pores developed in organic

Abbreviations: iCLEM, integrated correlative light and electron microscopy; SEM, scanning electron microscopy; PSD, pore size distribution; VR_o, vitrinite reflectance; BR_o, solid bitumen reflectance; PA, Pore area in scanning electron microscopy image.

* Corresponding author. School of Geoscience and Technology, Southwest Petroleum University, Chengdu, Sichuan, 610500, China.
E-mail address: hanhuigeology@163.com (H. Han).

https://doi.org/10.1016/j.petsci.2022.08.031

matter (Loucks et al., 2009). The proportion of OM pores in shale pores can reach 40% (Chalmers and Bustin, 2007, Chalmers et al, 2012; Curtis et al., 2010; Sondergeld et al., 2010). Han et al. (2019) indicated that the relative contribution of OM pores to total pore volume could reach 88.73%. Many studies have found a positive correlation between total organic carbon (TOC) and gas content or methane capacity (Strąpoć et al., 2010; Ma et al., 2015). Therefore, OM pores are generally considered to be primary storing space for hydrocarbons in shales (Ross and Bustin, 2009).

Most of the existing work on the development characteristics and controlling factors of OM pores is conducted on marine shale (Curtis et al., 2012; Milliken et al., 2013; Loucks and Reed, 2014; Wang et al., 2016; Hu et al., 2017, 2020; Liu et al., 2017; Ji et al., 2017, 2019; Chen et al., 2019; Zhang et al., 2020a). Although a few studies have been conducted on OM pores in lacustrine shales, most of them still remain in the description of morphology and size characteristics (Chen et al., 2016; Wang et al., 2018, 2020; Bai et al., 2022; Kuang et al., 2022; B. Liu et al., 2022). OM pores were rarely studied in the view of macerals. At present, some studies have found that the pore developments of various macerals were very different with each other in the same shale sample (Curtis et al., 2011, 2012; Sanei et al., 2015). The pore characteristics of dominant macerals in marine shales have been relatively well investigated, including fusinite (Curtis, 2002), sapropelinite, amorphous (Pacton et al., 2006; Löhr et al., 2015), graptolite (Luo et al., 2016; Ma et al., 2016; Guan et al., 2019), acritarch (Borjigin et al., 2021) and chitinozoan (Ardakani et al., 2018). However, it is well known that macerals in lacustrine shales are much more complex than marine shales. And the lacustrine shales are widely developed in China, such as Chang 7 shale of the Ordos Basin. A few initial works showed that there is a great hydrocarbon potential in Chang 7 shale (Yang et al., 2013; Lei et al., 2015; Fu et al., 2020). Guo et al. (2018) tried to utilize scanning electron microscopy (SEM) and optical microscopy to describe the pore development characteristics of solid bitumen and inertinite of Chang 7 shale in the Ordos Basin. Nevertheless, the pore development of the sapropelinite, liptinite and vitrinite in this lacustrine shale remain poorly understood.

In addition, the reflectance of vitrinite and solid bitumen in organic matter is considered to be the most reliable parameter to reflect thermal maturity of sedimentary organic matter (Taylor et al., 1998; Corcoran and Doré, 2005; Dembicki, 2009; Suárez-Ruiz et al., 2012). Besides thermal maturity, the reflectance of vitrinite or solid bitumen is also affected by other factors, such as bacterial degradation (Hartkopf-Fröder et al., 2015; Synnott et al., 2016), measuring probe size (Sanei et al., 2015), surface quality (Borrego et al., 2006), and associated minerals (Bostick and Alpern, 1977). Nonetheless, the effect of OM pores development on reflectance measurement of vitrinite and solid bitumen is still unclear.

At present, argon ion polishing technology combined with SEM is the main method to directly observe OM pores (Loucks et al., 2009, 2012; Milliken et al., 2013; Han et al., 2016a; Klaver et al., 2016; Cardott and Curtis, 2018; Hu et al., 2021). Although it is easy to identify OM in the backscattered electron (BSE) mode of SEM, various macerals cannot be distinguished only by the difference of morphology and grayscale in SEM images. Cardott and Curtis (2018) proved that the relatively enriched macerals in coal can be distinguished by using the subtle differences of grayscale under SEM with low magnification (650–1000 $\times$) and high accelerating voltage (10 kV), while the highly dispersed macerals in shale is difficult to identify under this condition. The macerals are mainly identified based on the color, transmittance, size, morphology, internal structure and reflectance of the organic matter under optical microscope (Stach et al., 1982; Taylor et al., 1998). Therefore, many researchers have tried to combine optical microscopy and SEM to research the pore development characteristics of different macerals (Bernard et al., 2012; Fishman et al., 2012; Baruch et al., 2015; Cardott et al., 2015; Luo et al., 2016; Ma et al., 2016; Liu et al., 2017, 2022; Guo et al., 2018; X.P. Liu et al., 2022). However, because there are often tens to hundreds of nanometer to micrometer organic matter in shales, it is very difficult to relocate organic matter between the instrument conversion and the sample is also vulnerable to damage (Timmermans and Otto, 2015; Guo et al., 2018). Integrated correlative light and electron microscopy (iCLEM) system, which can realize the observation of optical microscope and SEM in the same experimental instrument without sample transfer, has been widely used in cellular biology research (Polishchuk et al., 2000; De Boer et al., 2015). Hackley et al. (2017) have applied iCLEM system to characterize the microstructure of macerals of the Bakken Shale from North Dakota, USA, and have shown a good result. In addition, due to the 5 nm resolution of SEM (Chalmers et al., 2012), about 60%–90% of OM pores could not be observed under SEM (Milliken et al., 2013). Low-pressure gas (carbon dioxide and nitrogen) adsorption (LPGA) experiments can realize the quantitative characterization of pores in the diameter range of 0.35–200 nm (Chalmers and Bustin, 2015; Han et al., 2016a). Among them, LPGA-N_2 (Sing, 2001; Yang et al., 2014) is suitable for characterizing meso- and macropores, and LPGA-CO_2 (Han et al., 2016a; Wei et al., 2016; Cao et al., 2019) is applicable for describing micropores (Bustin et al., 2008). LPGA experiments have been extensively applied in the pore characterization of kerogen samples (Rexer et al., 2014; Teng et al., 2017; Han et al., 2018; Pang et al., 2018), which can make up for the defect of resolution of iCLEM in the observation of OM pores to a certain extent.

In this study, 10 typical lacustrine shale samples with different TOC contents and maturities were selected from Chang 7 member of Yanchang Formation in the Ordos Basin, China. OM pores of different macerals were characterized using iCLEM and LPGA experiments. Furthermore, the reflectance at different positions of the same vitrinite or solid bitumen with nonhomogeneous pore development were also analyzed. Based on these results, the pore characteristics of various macerals and the effect of OM pores on reflectance measurement were revealed.

2. Geological settings and samples

The Ordos Basin is located in the west of North China Platform with a total area of about 32 $\times$ 10^4 km^2, which is divided into six tectonic units: Yimeng uplift, Tianhuan depression, Western edge thrust belt, Weibei uplift, Jinxi fault-fold belt and Yishan slope (Xiao et al., 2005; Guo et al., 2018) (Fig. 1a). The Yanchang Formation is further subdivided into 10 members, ranging from Chang 1 to Chang 10 from top to bottom (Han et al., 2019) (Fig. 1b). Chang 7 member developed in the deep lake and semi-deep lake sedimentary environment of typical continental lake, whose lithologic combination is black or gray black oil shales and carbonaceous shales (Sun et al., 2015; Jiang et al., 2016) (Fig. 1b). As one of the main hydrocarbon source rocks in the Ordos Basin, Chang 7 member shows a significant potential in shale oil and gas (Lei et al., 2015). In our study, ten shale samples belonging to Chang 7 member were collected from wells Yan 56, Huan 317, Zhuang 233, Zheng 3, Honghe 21 and Jinghe13 (Fig. 1a).

3. Methods

3.1. Geochemical and mineralogical measurements

The determination of TOC content was carried out in a carbon-

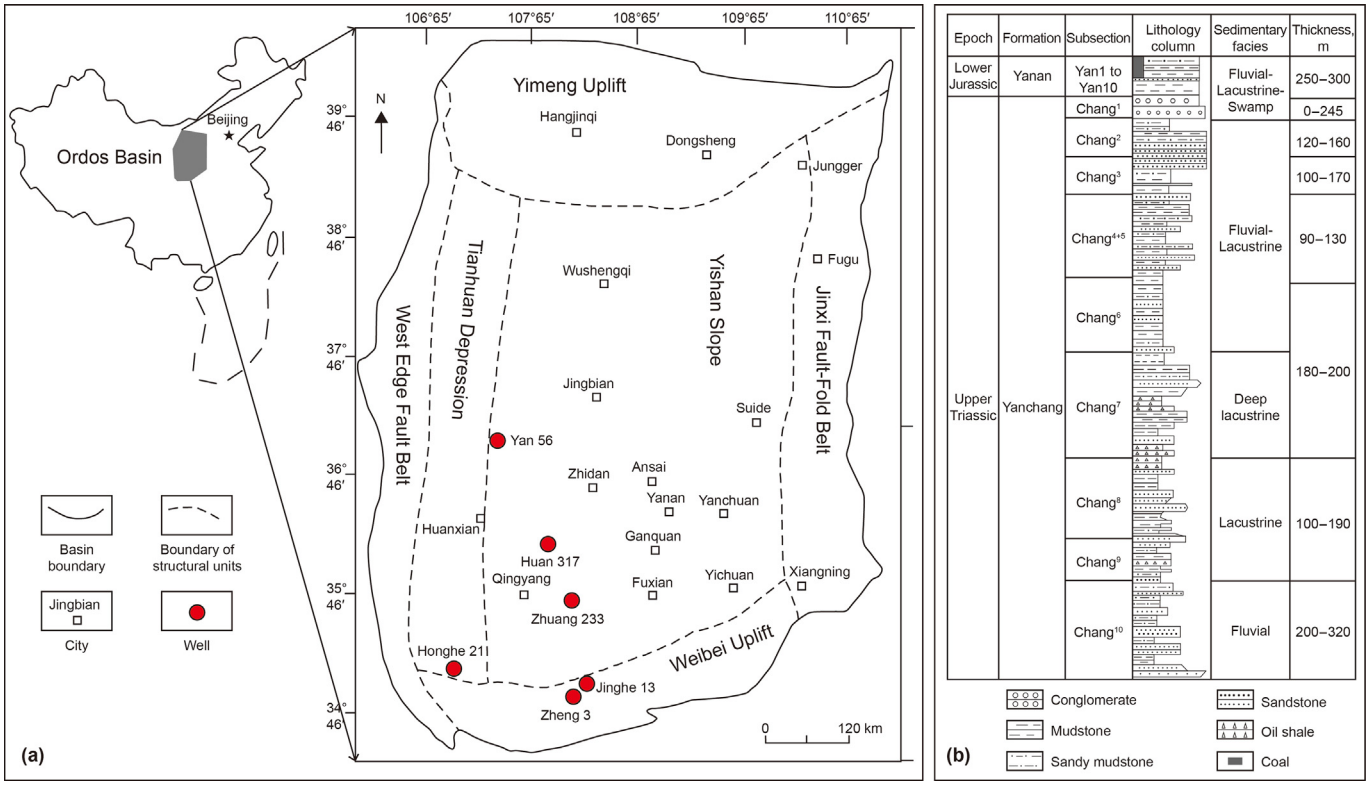

Fig. 1. Location and tectonic units of the Ordos Basin (a), and lithology column of Yanchang Formation (b) (based on Pang et al., 2021).

Table 1
Data sources and calculation methods of different pore structure parameters.

Parameters	Data	Models
Pore volume and surface area of micropore	CO_2 adsorption branch	Dubinin-Radushkevich (DR)
Pore volume and surface area of meso- to macropore	N_2 adsorption branch	Barrett-Joyner-Halenda (BJH)
PSD (~1.5 nm)	CO_2 adsorption branch	Density functional theory (DFT)
PSD (1.5–200 nm)	N_2 adsorption branch	Barrett-Joyner-Halenda (BJH)

sulfur analyzer (CS-230) produced by LECO. A Rock-Eval II instrument was utilized for pyrolysis analysis to powdered samples (100 mesh). And, the equivalent vitrinite reflectance (Eq-R_o) was used to characterize organic matter maturity of samples. This parameter was calculated by Eq. (1), which is applicable to type III or type II organic mattes (Jarvie et al., 2001).

$$\text{Eq-}R_o = 0.0180 \times T_{max} - 7.16 \quad (1)$$

Peters et al. (2005) had proved that the calculated values of Eq-R_o are in good agreement with the actual measured values of vitrinite reflectance. Finally, the mineral composition of shale samples was tested in the TTR III multifunctional X-ray diffractometer.

3.2. iCLEM

Firstly, the shale samples cut into small cubes (1 cm × 1 cm × 0.3 cm) were polished by argon ion using Leica

Table 2
Geochemical parameters of Chang 7 shale samples.

Sample	Well	Depth (m)	TOC (w.t.%)	S_1 (mg/g)	S_2 (mg/g)	T_{max} (°C)	HI (mg/g TOC)	Eq-R_o (%)
1	Zheng3	866.74	2.89	0.62	15.16	437	397	0.71
2	Zhuang233	1798.7	25.10	10.43	135.13	439	538	0.74
3	Jinghe13	1357.23	1.46	0.29	5.68	440	302	0.76
4	Zhuang233	1790	6.22	2.11	25.30	443	407	0.81
5	Honghe21	1676.69	0.46	0.15	0.36	444	67	0.83
6	Yan56	2963.1	6.09	2.98	14.91	446	245	0.87
7	Yan56	2978.5	6.29	3.02	15.88	450	252	0.94
8	Yan56	2996.5	6.25	3.11	14.32	452	229	0.98
9	Huan317	2468.3	18.10	4.81	36.07	456	199	1.05
10	Huan317	2474.3	7.95	2.78	9.89	466	124	1.23

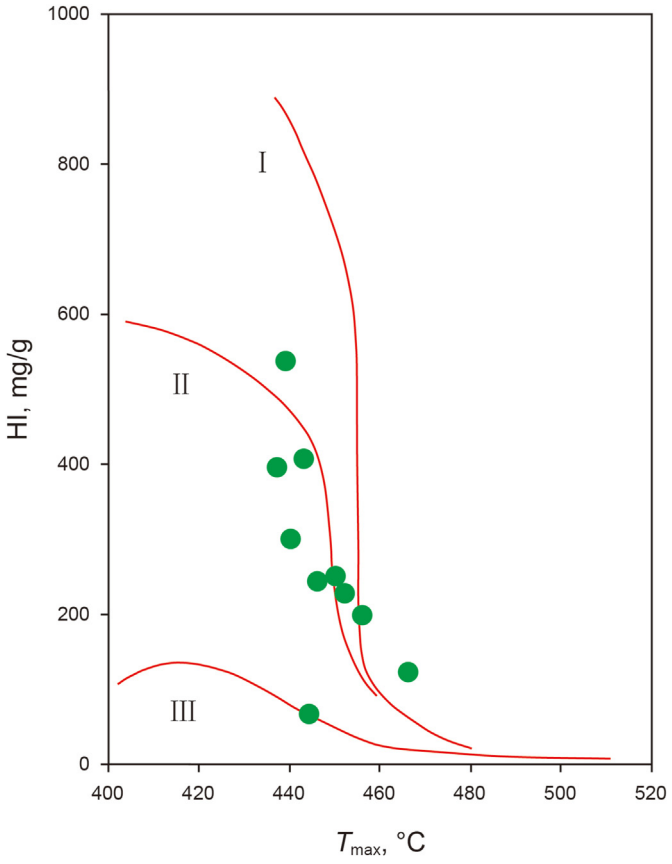

Fig. 2. T_{max} vs. HI diagram of Chang 7 shales (based on Espitalie et al., 1985).

EMTIC3X instrument. Then, the prepared samples were placed under LEICA DM 4500 P polarizing microscope, and the macerals were identified under reflection light and fluorescence excited by blue light, respectively. The magnification of the optical microscope is 50–400 times. The pores of macerals were observed by Quanta 650 FEG SEM produced by FEI. The working voltage was 10 kV, the working distance was 10 mm. Finally, the pore numbers and plane porosities of each maceral were obtained from SEM images by using the JMicroVision image analysis software.

3.3. Organic matter isolation

Based on the demand for quantitative characterization of OM pore, shale samples will be addressed to obtain their kerogen samples utilizing the standard method recommended by Rexer et al. (2014). First, 10–20 g fresh comminuted samples (60 mesh) were processed with 5–20 mL hydrochloric acid for 12 h to remove carbonate minerals. And, the mixture was diluted with degassed water, centrifuged (15 min, 3500 r/min) for 3 times and freeze-dried (~25 °C). The freeze-dried samples were then soaked with 15 mL hydrofluoric acid for 12 h to remove silicate minerals, and diluted again with degassed water. Finally, a qualitative filter paper with 25 μm particle retention was used to filter organic matters. Considering that soluble organic matter also contains a large number of pores (Milliken et al., 2013), in our study, chloroform bitumen ' A ' was not removed by Soxhlet extraction.

3.4. LPGA

The crushed samples (60 mesh, Han et al., 2016b) were firstly dried and degassed under a high vacuum (<10 mmHg) and high temperature (110 °C) condition for more than 12 h (Tian et al., 2013). LPGA experiments were performed on 1–2 g prepared samples by utilizing a Micromeritics ® ASAP 2020 instrument. Studied samples were then exposed to N_2 or CO_2 at ~196.15 °C or 0 °C, respectively. In the end, the amounts of absorbed N_2 and CO_2 were calculated in the relative pressures (P/P_0) ranges of

Table 3
Mineral composition of Chang 7 shale samples.

Sample	Relative percent (w.t.%)								Relative clay percent (w.t.%)			
	Quartz	Feldspar	Calcite	Dolomite	Pyrite	Siderite	Aragonite	Clays	I/S	Illite	Kaolinite	Chlorite
1	26	8.9			9.5			55.6	59	20	8	13
2	23.44	6.91				40.98		28.67	70	22	3	5
3	43.2	11.4	0.8	4.7				39.9	64	22	2	12
4	45.82	6.44				17.68		30.06	77	16	2	5
5	23.5	17.2		3				56.2	31	29	19	21
6	24	15.3			2.1	1.3	13.8	43.5	53	18	13	16
7	29.3	10.8				4		55.9	57	17	12	14
8	31.5	12.5				6.6		49.4	64	17	11	8
9	22.13	8.2	2.27			19.04		48.36	69	25	3	3
10	24.82	9.29				5.24		60.65	71	21	4	4

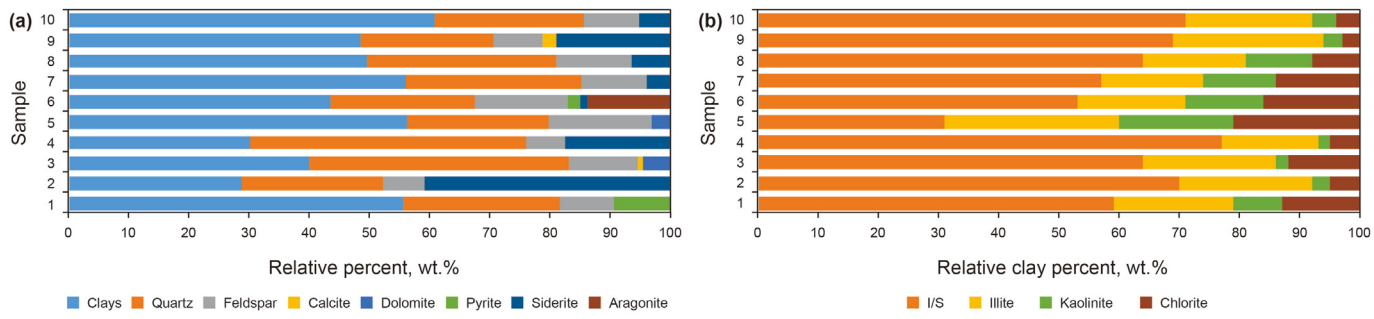

Fig. 3. Bar graph of mineral contents of Chang 7 shale samples.

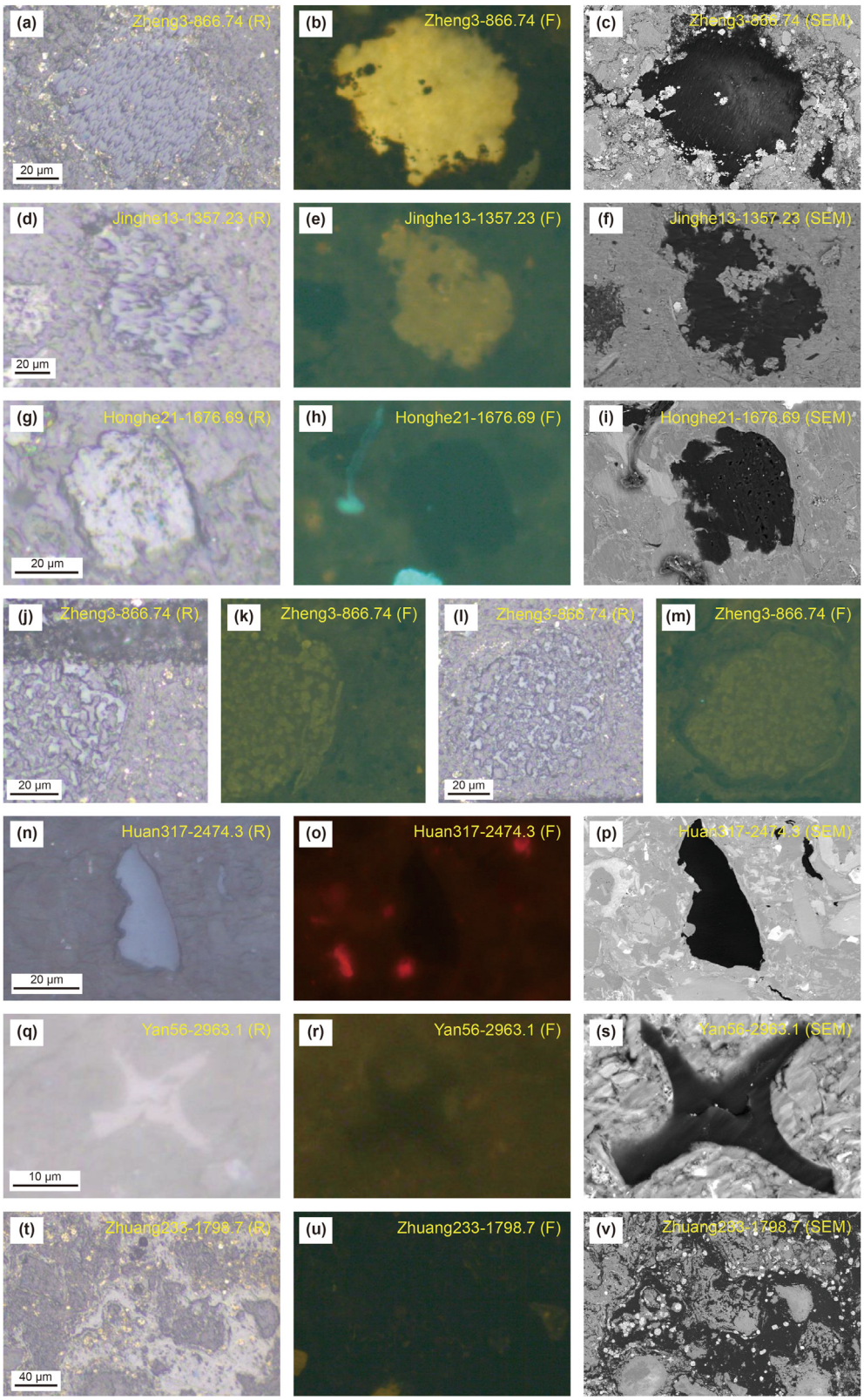

Fig. 4. Characteristics of macerals in Chang 7 shale under reflected light, fluorescence and scanning electron microscope (a–c: alginite; d–f: saprolite hydrogen-rich bituminite; g–i: humic hydrogen-poor bituminite; j–m: liptinite; n–p: vitrinite; q–s: fusinite; t–v: mineral bitumen matrix; R: reflected light; F: fluorescence; SEM: scanning electron microscopy).

Table 4
Compositions of macerals for the studied samples.

Sample	Sapropelinite (%)		Liptinite (%)			Vitrinite (%)	Inertinite (%)	Solid bitumen (%)	Mineral bituminous matrix (%)
	Alginite (%)	Bituminite (%)	Sporinite (%)	Cutinite (%)	Resinite (%)				
1	9.21	42.11	5.26	1.32	1.32	15.79	18.42	6.58	
2	8.57	22.86	1.43	2.86		15.71	12.86	24.29	11.43
3		38.18	3.64	5.45		5.45	12.73	29.09	5.45
4		30.77	7.69		2.56	5.13	5.13	48.72	
5		52.38	7.14	4.76		16.67	16.67	2.38	
6		46.48	1.41	8.45	1.41	16.90	18.31	7.04	
7		59.18	4.08			14.29	8.16	14.29	
8	7.69	23.08	2.56		2.56	2.56	7.69	53.85	
9		34.15	4.88	2.44	4.88	21.95	17.07	4.88	9.76
10		42.86	5.71	2.86		17.14	17.14	14.29	

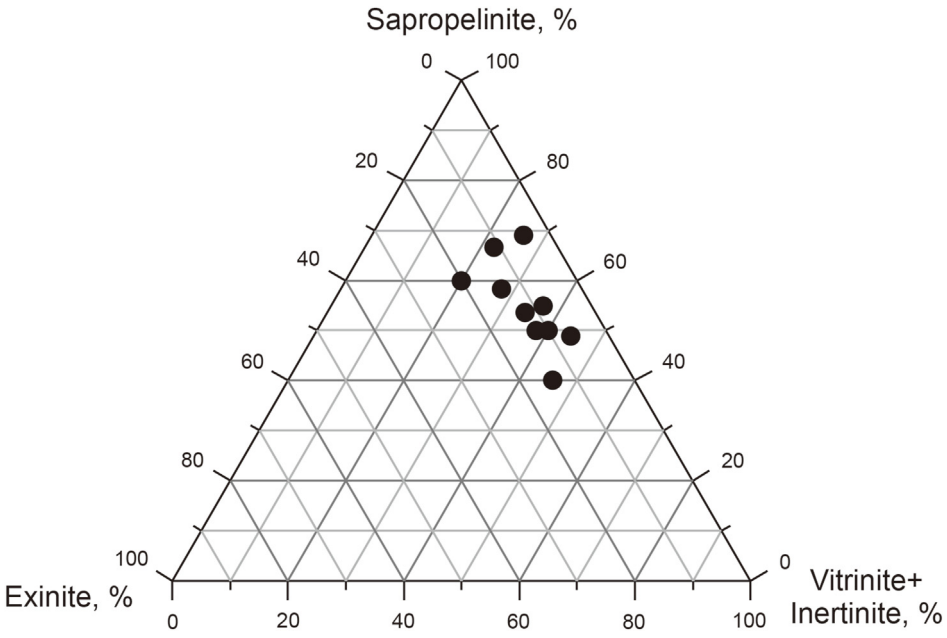

Fig. 5. Ternary diagram of organic maceral composition in Chang 7 shales.

0.05–0.995 and 0.0005–0.03, respectively. The pore size ranges characterized by LPGA-N_2 and LPGA-CO_2 are 1.7–200 nm and 0.3–1.5 nm, respectively (Cao et al., 2016). So, in our study, CO_2 and N_2 were utilized to discribe pore structure of micropore (<2 nm) and meso-to macropore (2–200 nm) of studied samples, respectively. The data sources and calculation models of different pore structure parameters are shown in Table 1.

3.5. Reflectance measurement

In our study, the reflectance of vitrinite and solid bitumen (VR_o and BR_o) was tested on a MPV-III microphotometer with input voltage of 220 V and magnification of × 500 at 23 °C. The wavelength and refractive index of the incident light are 546 ± 5 nm and 1.5180 + 0.0004, respectively.

4. Results

4.1. Geochemistry

The organic geochemical information of studied sample was shown in Table 2. TOC contents were distributed in the range of 0.46–25.1 w. t.% and averaged 8.08 w. t.%. The equivalent vitrinite reflectance (Eq-R_o) ranged from 0.71% to 1.23%. The OM type was analyzed by T_{max} vs. HI chart (Espitalie et al., 1985). The results showed that the OM types were mainly type II in the ten Chang 7 shale samples (Fig. 2).

4.2. Mineral composition

The experimental results of mineral composition of Chang 7 shales were shown in Table 3 and Fig. 3. Among them, the contents of clay minerals, quartz and feldspar were distributed in the range of 28.67%–60.65%, 22.13%–45.82% and 6.44%–17.20%, and their average contents were 46.82%, 29.37% and 10.69%, respectively (Fig. 3a). The clay minerals are dominated by mixed-layer minerals of illite and smectite, accounting for 31%–77% of the total clay minerals and averaging 61.5% (Fig. 3b).

4.3. Organic macerals composition

In this paper, the macerals of Chang 7 shale were identified by analyzing the characteristics of organic matter under reflection light and fluorescence of optical microscope. At the same time, the gray scale, morphological characteristics, contact relationship and occurrence state of macerals under scanning electron microscope

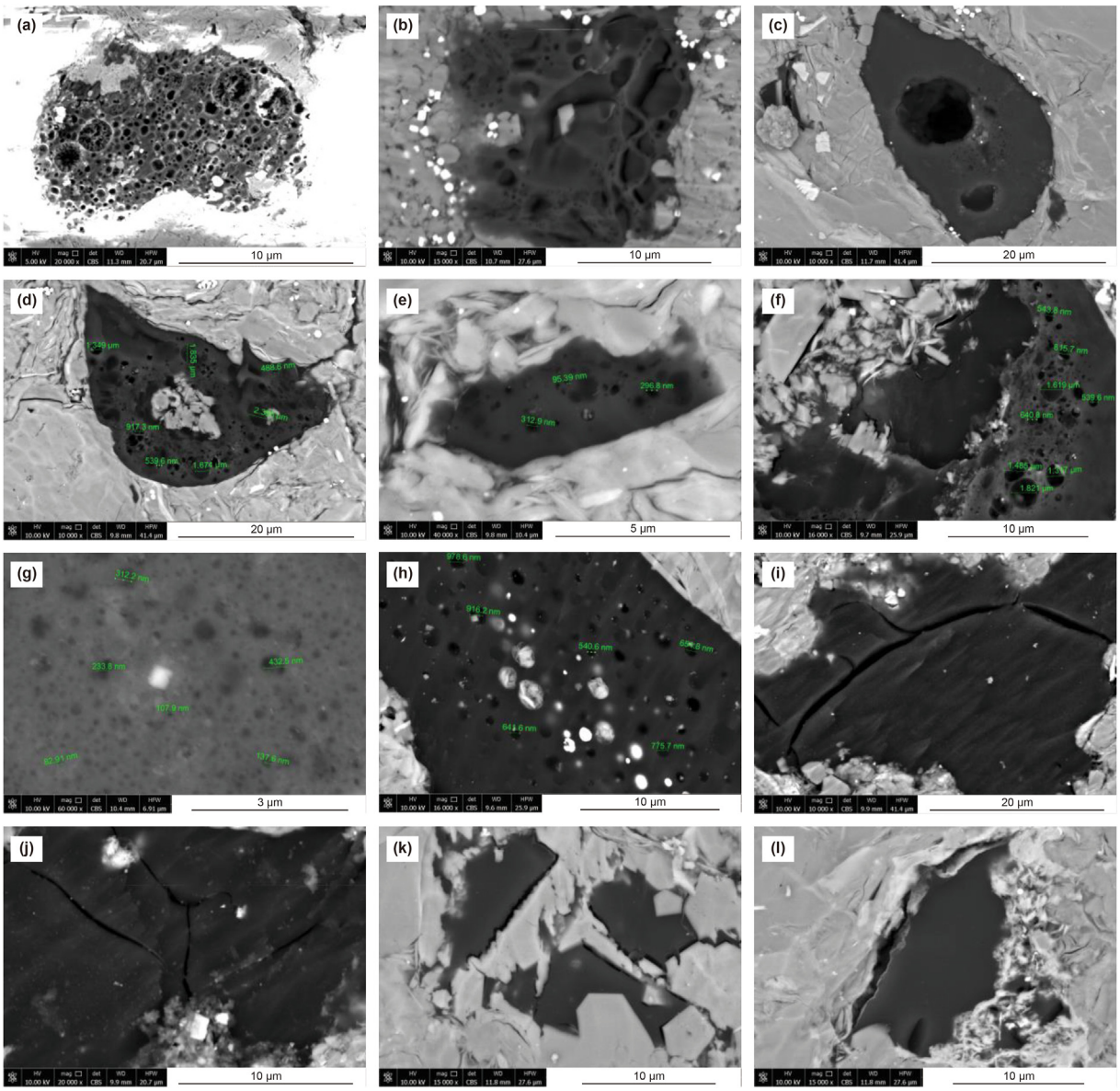

Fig. 6. Characteristics of OM-related pores in Chang 7 shale. (a, Yan56–2996.5; b, g, Zhuang233-1790; c, Jinghe13–1357.23; d, e, f, Zheng3-866.74; h, Zhuang233–1798.7; i, j, Yan56–2963.1; k, l, Jinghe13–1357.23).

can also be used as auxiliary identification basis.

The sapropelinite of studied samples was mainly composed of alginite and bituminite. Alginite were mostly oval in shape, dark gray and strongly protruding under the reflected light. Its fluorescence was strong and bright yellow. Under the electron microscope, wrinkles and decorations were often observed on the surface (Fig. 4a–c). Bituminite were mostly interstitial or lumpy in shape, and appear gray or white under reflected light, with slight protrusions. And, bituminite can be subdivided into yellow fluorescent saprolite hydrogen-rich bituminite (Fig. 4d–f) and non-fluorescent humic hydrogen-poor bituminite (Fig. 4g–i). In this study, bituminite is the degradation product of low aquatic plankton, bacteria and algae, which belongs to pre-oil bitumen.

The shape of liptinite often retained the plant tissue structure, which was mostly clastic or banded distribution, and the outline was clear. And, liptinite was gray and protuberant under reflected light. Weak yellow fluorescence was observed under blue light (Fig. 4j–m).

The vitrinite of studied samples were gray, low protrusions, no fluorescence or weak fluorescence under optical microscope, whose morphology was mostly angular or rod-like. Moreover, vitrinite had flat, homogeneous and shell-like fracture morphology under scanning electron microscope (Fig. 4n–p).

The inertinite of Chang 7 shale was mostly fusinite, and its morphology retained many plant tissue structures. Under the irradiation of reflected light, it was white, no protrusions, and no fluorescence (Fig. 4q–s).

In addition, secondary products and a small amount of mineral bitumen matrix were found in Chang 7 shale. Secondary products were mainly composed of solid bitumen, which was the cracking product of crude oil and belongs to post-oil bitumen. Mineral bitumen matrix is a collection of inorganic minerals and organic matter, which is not a maceral with conventional definition. Under optical microscope, mineral bitumen matrix was no fixed form, gray, no fluorescence. Under scanning electron microscope, it was uniformly mixed with minerals and distributed continuously

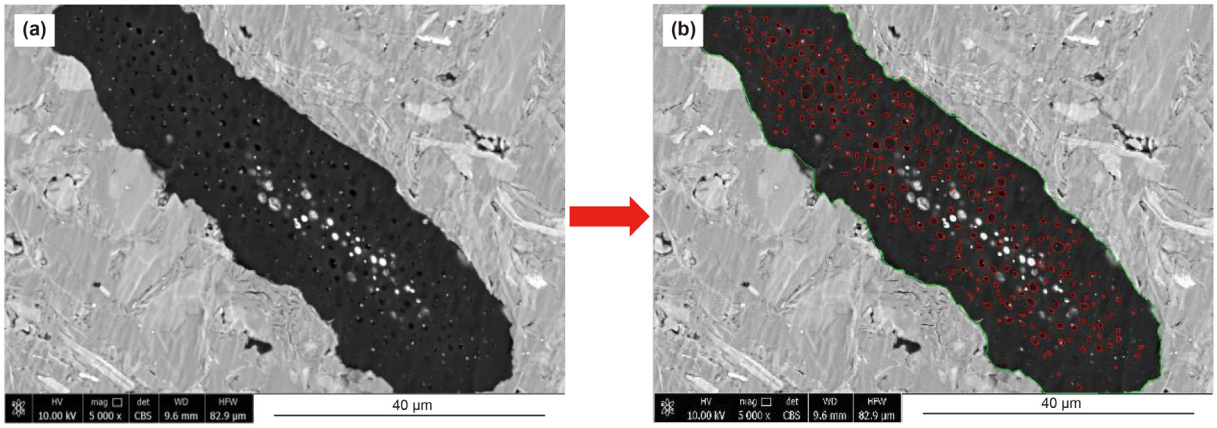

(c) Area, m²	Perimeter, m	Length, m	Width, m	Equivalent circular diameter, m	Class
1.54E-09	2.01E-04	8.51E-05	2.54E-05	4.42E-05	OM
3.66E-12	6.80E-06	2.46E-06	1.98E-06	2.16E-06	OM pore
2.74E-12	6.21E-06	2.31E-06	1.36E-06	1.87E-06	OM pore
2.51E-12	5.58E-06	1.80E-06	1.62E-06	1.79E-06	OM pore
2.44E-12	5.54E-06	1.98E-06	1.57E-06	1.76E-06	OM pore
2.41E-12	5.50E-06	1.89E-06	1.63E-06	1.75E-06	OM pore
1.68E-12	4.68E-06	1.87E-06	1.22E-06	1.46E-06	OM pore
.....	.....	.....	.....	.....	.....

Fig. 7. Process of JMicroVision treating organic pores in SEM images. (a: Original SEM image; b: Organic pores were identified by JMicroVision; C: Pore structure parameter table derived from JMicroVision).

Table 5
Statistical results of organic pores in the studied samples.

Sample	OM counts	Pore counts	Average pore diameter (nm)	Plane porosity (%)
1	76	666	471.69	21.62
2	70	55	891.49	3.23
3	55	263	593.19	7.23
4	39	557	331.85	10.46
5	42	693	611.77	2.40
6	71	292	614.42	9.43
7	49	581	913.36	8.07
8	39	2748	185.82	12.78
9	41	358	280.67	10.60
10	35	1578	304.56	15.43

(Fig. 4t–v).

Different macerals in Chang 7 shale samples were identified and counted in detail (Table 4, Fig. 5). The contents of sapropelinite, liptinite, vitrinite, inertinite and solid bitumen were in the ranges of 30.8%–59.2%, 4.1%–13.5%, 2.6%–24.3%, 5.1%–18.9% and 2.4%–53.8%, respectively. The results indicate that the main source of OM in Chang 7 shale is a mixture of lacustrine lower hydrobionts, such as algae, and terrigenous higher plant, which is consistent with the research of Qiao et al. (2021).

4.4. OM pore characteristics under FE-SEM

4.4.1. Pore type

Under the backscatter mode of SEM, amounts of organic pores and fractures were observed in Chang 7 shale. Based on pore morphology, location and genesis, OM-related pores are divided into three types in this study: OM intragranular pores, OM internal microcracks and OM marginal shrinkage cracks. OM intragranular pores are mostly round or elliptical, usually densely distributed in honeycomb shape (Fig. 6a–h). Their pore sizes are mostly more than 100 nm (Fig. 6d–h), and even some can reach 10 μm (Fig. 6c). Microcracks in OM are mostly curved and interlaced, with widths of hundreds of nanometers and lengths of more than 10 μm (Fig. 6i and j). The average density of microcracks is about 3–5 piece. OM marginal shrinkage cracks are developed at the contact edges of organic matters and inorganic minerals in a straight, serrated or angular edge shape (Fig. 6k and l). Most of them are hundreds of nanometers in width and more than 10 μm in length.

4.4.2. Pore size distribution and plane porosity

In our research, based on SEM images, the pore number and pore size of each piece of OM of shale samples were counted in

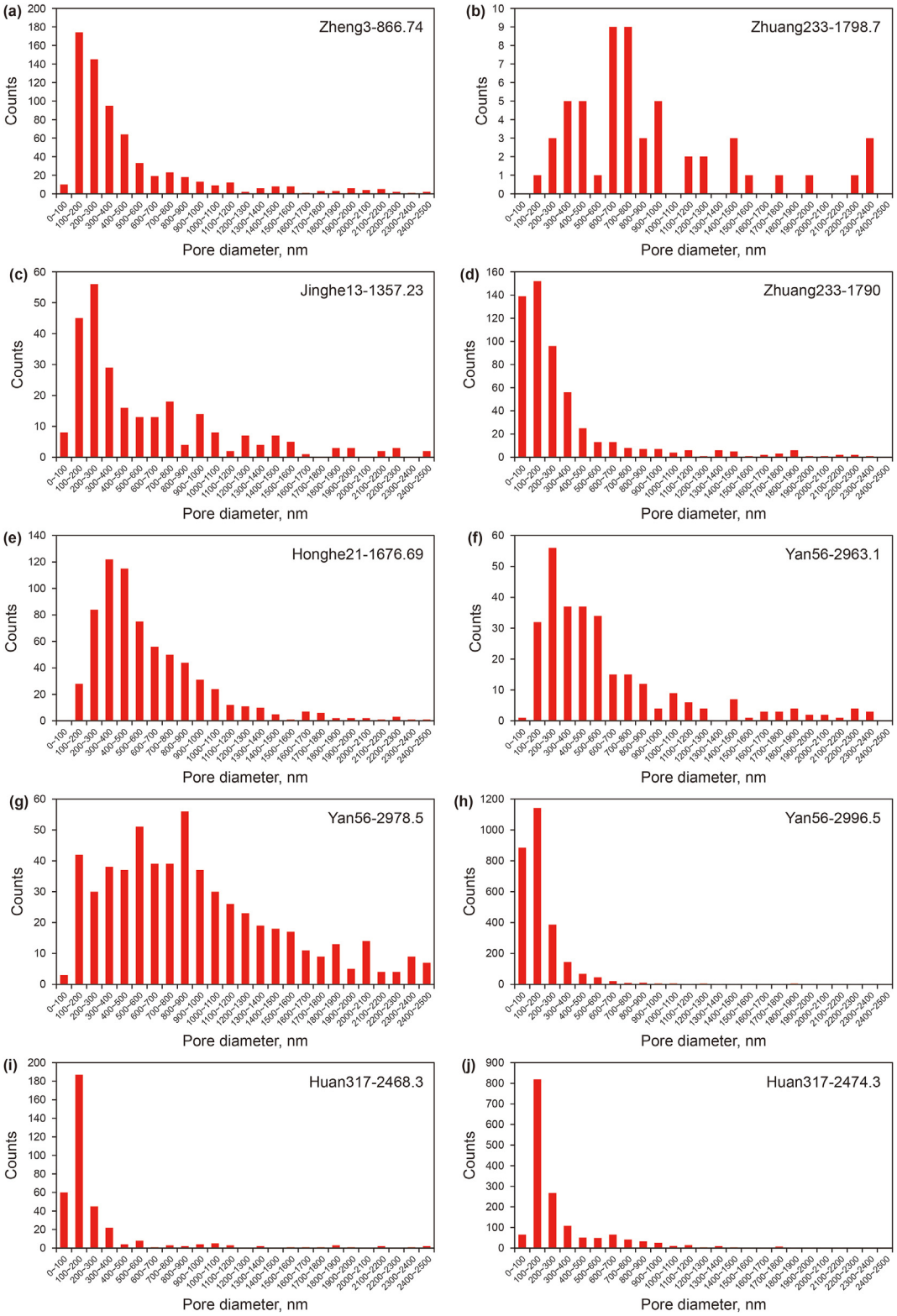

Fig. 8. Histograms of PSD of organic pores in the studied samples.

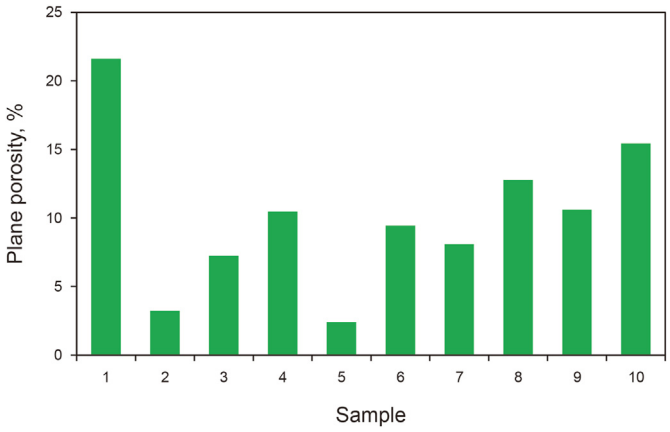

Fig. 9. The plane porosities of OM pores in Chang 7 shale.

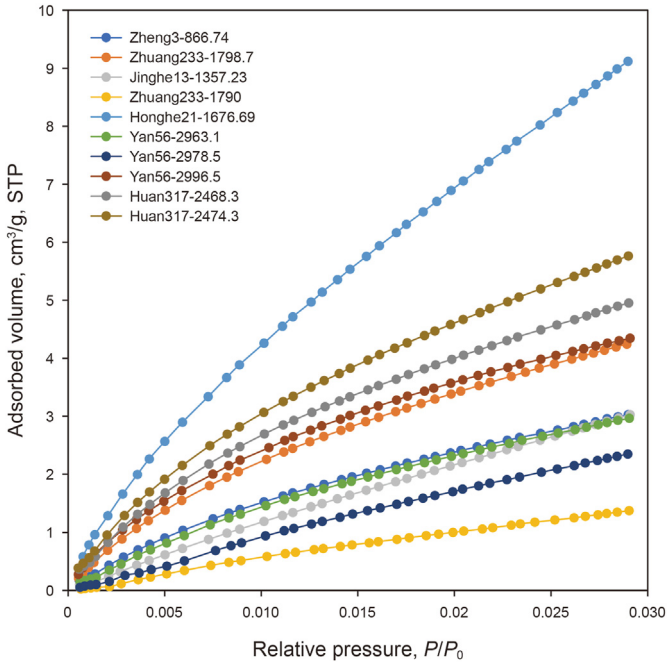

Fig. 10. LPGA-CO_2 isotherms for our OM samples.

detail using JMicroVision software (Fig. 7). The statistical results were shown in Table 5 and a histogram of pore size distribution (PSD) of OM pores of ten shale samples was plotted in Fig. 8. The average pore diameter of OM pores ranges from 185.82 nm to 913.36 nm. Under SEM, the size of OM pores is widely distributed in the range of 5 nm–2.5 μm. Almost all PSDs show an obvious single-peak pattern with strong left deviation, and the main peaks of PSDs of organic pores ranges from 100 nm to 500 nm. Except for sample 2 (Fig. 8b), whose result of PSD is unrepresentative due to the lack of organic pore (Table 5).

The plane porosities of organic pores of the studied samples were shown in Table 5 and Fig. 9, with a range of 2.40%–21.62% and an average of 10.13%.

4.5. OM pore characteristics revealed by LPGA

4.5.1. Isotherms

The LPGA-CO_2 isotherms of the studies sample can be seen in Fig. 10. All of them began to adsorb at very low relative pressure.

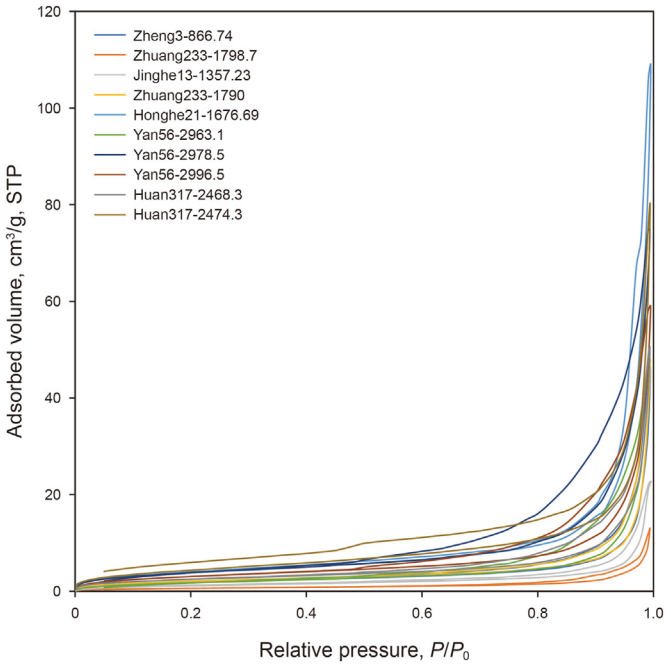

Fig. 11. LPGA-N_2 isotherms for our OM samples.

The morphology of isotherms is concave towards P/P_0 axis, and the adsorbed amounts of carbon dioxide for organic matter samples ranged from 1.5 cm^3/g to 10 cm^3/g. The LPGA-CO_2 isotherms of all OM samples are type I in accordance with the IUPAC classification method (Brunauer et al., 1940), indicating that the organic sample was a microporous solid with a relatively small outer surface (Sing et al., 1985).

The LPGA-N_2 isotherms of the studied sample were shown in Fig. 11. In morphology, all curves are convex to the P/P_0 axis, and the adsorbed amounts of nitrogen for organic matter samples ranged from 15 cm^3/g to 120 cm^3/g. In the light of IUPAC classification, the LPGA-N_2 curves of all OM samples are type IV (Brunauer et al., 1940), which represents the adsorption behavior of mesopores. The isotherms of this type all have a hysteresis loop induced by capillary condensation that occurs in the mesoporous structure (Sing et al., 1985), whose desorption curves include a steep section closed with the adsorption branch (Fig. 11). These hysteresis loops of OM samples in Chang 7 member are type H_3 on the basis of IUPAC classification, indicating the existence of uneven slit-shaped pores. This is consistent with the phenomenon observed under SEM (Fig. 6i–l).

4.5.2. Surface area and pore volume

The surface areas and pore volumes of OM samples calculated from LPGA data are shown in Table 6 and Fig. 12, and these pore structure parameters in the macropore (50–200 nm), mesopore (2–50 nm) and micropore (<2 nm) ranges are listed separately. The surface areas of micropores, mesopores and macropores varied in the range of 1.83–74.19 m^2/g, 1.22–9.62 m^2/g and 0.48–4.68 m^2/g, respectively. The pore volumes of macropores, mesopores and micropores in the ranges of 0.0149–0.135 cm^3/g, 0.0049–0.0397 cm^3/g and 0.0010–0.0250 cm^3/g, respectively.

4.5.3. Pore size distribution

PSDs of OM Samples of Chang 7 shale can be seen in Fig. 13. The PSDs in the range of ~1.5 nm and 1.5–200 nm were calculated using CO_2 adsorption data and N_2 adsorption branch, respectively. Two

Table 6
Surface areas and pore volumes of OM in Chang 7 shale.

Sample	Surface area (m^2/g)				Pore volume (cm^3/g)			
	Micropore	Mesopore	Macropore	Total	Micropore	Mesopore	Macropore	Total
1	39.61	3.19	1.89	44.69	0.013	0.0122	0.0584	0.0836
2	54.47	1.22	0.48	56.17	0.018	0.0049	0.0149	0.0378
3	7.46	2.24	1.05	10.75	0.002	0.0069	0.0278	0.0367
4	28.67	3.05	2.09	33.81	0.01	0.0112	0.0616	0.0828
5	1.83	7.64	4.86	14.33	0.001	0.0333	0.135	0.1693
6	47.37	3.77	2.31	53.45	0.016	0.0162	0.0602	0.0924
7	51.41	9.62	3.05	64.08	0.015	0.0397	0.0756	0.1303
8	52.03	6.00	2.41	60.44	0.017	0.0236	0.0661	0.1067
9	65.26	4.89	2.05	72.20	0.022	0.0191	0.054	0.0951
10	74.19	8.63	3.13	85.95	0.025	0.025	0.0962	0.1462

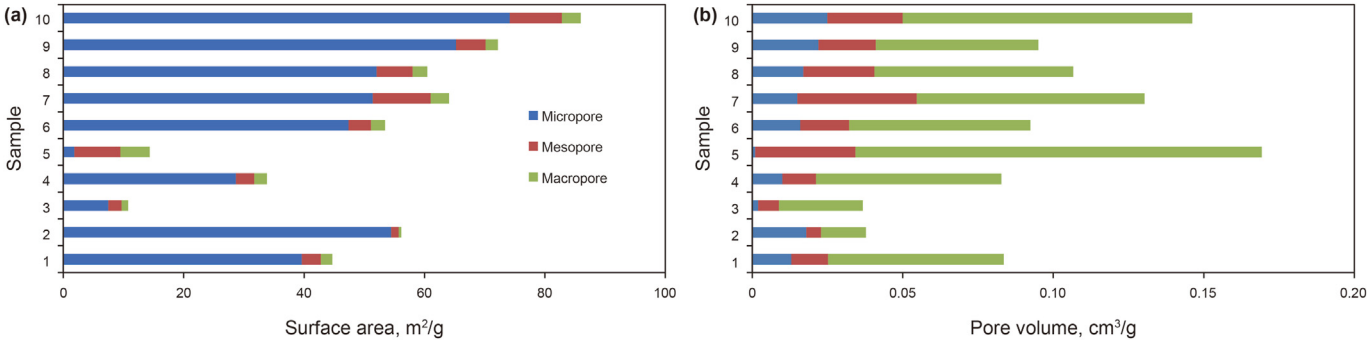

Fig. 12. Bar diagrams of surface areas and pore volumes of OM for Chang 7 shale (a: surface area; b: pore volume).

main peaks were present in the PSD curves of all OM samples at 0.6 nm and 0.8 nm.

4.6. Reflectance of vitrinite and solid bitumen (VR_o and BR_o)

In this study, the reflectance of the parts with different organic pore development in the same piece of vitrinite (sample No. 10) or the same piece of solid bitumen (sample No. 8) was measured and shown in Fig. 14 and Fig. 15, respectively. It can be found that the reflectivity measurements at the pores with larger pore size (Fig. 14a, r (b1) < r (b2) < r (b3)) are lower than that at the pores with smaller pore size in vitrinite (Fig. 14b, VR_o (b1) > VR_o (b2) > VR_o (b3)), and the VR_o difference between them is larger, reaching more than 0.5%. Similarly, in the same piece of solid bitumen, the reflectance measurements of parts with different pore development degrees (Fig. 15a, PA (b1) < PA (b2) < PA (b3), PA: pore area) are significantlly different (Fig. 15b, Eq-R_o > BR_o (b1) > BR_o (b2) > BR_o (b3)).

5. Discussion

5.1. Influence of macerals on pore structure

5.1.1. Qualitative observation

Differences in the pore development between two adjacent OM in the same view of SEM had been reported in some studies (Curtis et al., 2011, 2012; Sanei et al., 2015; Tian et al., 2015), suggesting that the type of macerals has a significant effect on the development of organic pores. Therefore, the pore development characteristics of various macerals in Chang 7 shale under SEM were discussed respectively, including sapropelinite (alginite and bituminite), liptinite (sporinite, cutinite), vitrinite, inertinite and solid bitumen.

5.1.1.1. Sapropelinite. Sapropelinite contains alginites and bituminite. The pore development characteristics of alginites and bituminite under SEM can be seen in Fig. 16 and Fig. 17, respectively. It can be found that the pores of alginite and bituminite are well developed, often showing a honeycomb aggregation form. The pore morphology is mostly round or oval, and the pore diameters are hundreds of nanometers. Moreover, the pores within OM have a good connectivity, many smaller pores can connect to form several organic pores with larger diameters (Fig. 16a). In addition, some microcracks were also developed in the interior of bituminite, with the width of hundreds of nanometers and the length up to 20 μm (Fig. 17g and h). Plenty of nanoscale pores of sapropelinite had been seen in the Longmaxi Shale with uneven size and dense distributions (Jia et al., 2021). The existing pores of OM in shales before entering the oil window were defined as primary organic pores, and the pores formed after entering the oil window were secondary organic pores (Curtis et al., 2012; Löhr et al., 2015). Some alginites in sapropelinite have original morphological characteristics (Fig. 16a), and similar primary pores exist in bituminite (Fig. 17a). Similarly, Pacton et al. (2006) and Löhr et al. (2015) found that the bituminite bodies in marine shales also developed primary pores to varying degrees. According to the phenomenon that most of organic pores are elliptical or circular, it is believed that the massive generation of natural gas is an important reason for the formation of OM pores (Milliken et al., 2013; Schieber, 2013; Pommer and Milliken, 2015). However, our observations suggest that the primary pores may also account for a relatively large proportion in sapropelinite.

5.1.1.2. Liptinite. The pore development characteristics of liptinite under SEM are shown in Fig. 18. The liptinite in Chang 7 shale consists of sporinites, cutinites and resinites. It can be found that the pores and microcracks of the liptinite in Chang 7 shales are rarely developed. At the same time, the maceral composition

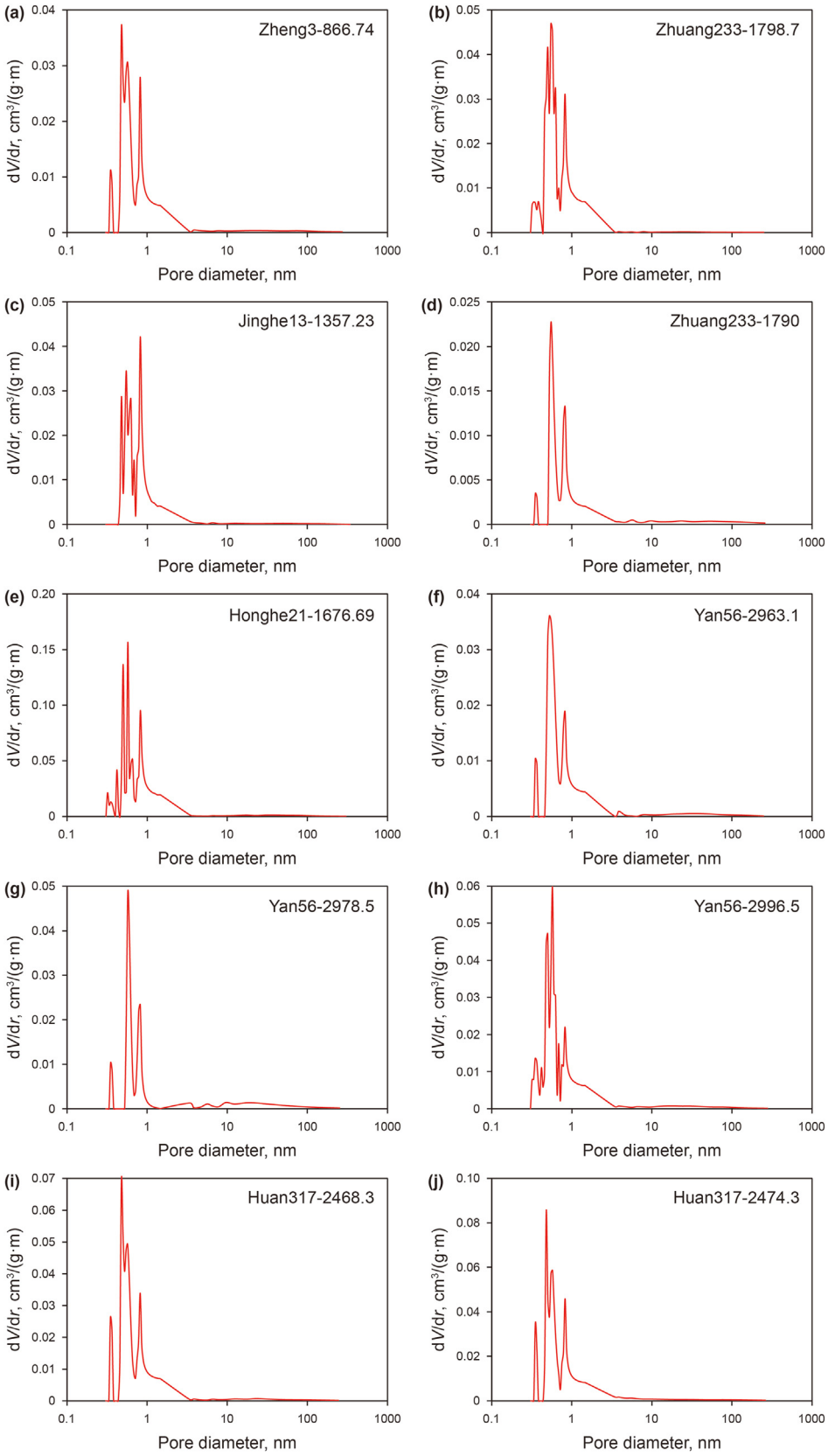

Fig. 13. The PSDs of OM samples in Chang 7 Shale.

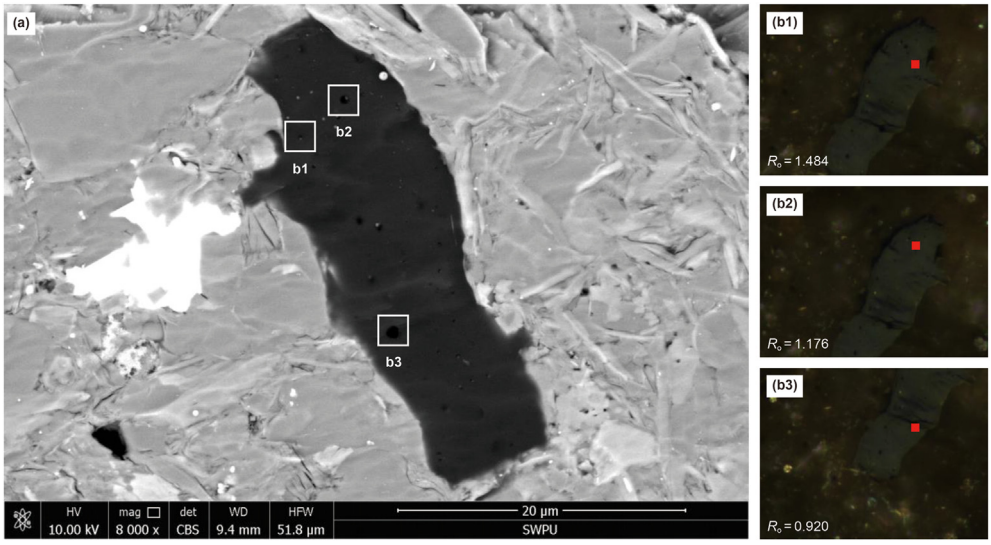

Fig. 14. Reflectance test values of vitrinite at different pore development locations. (r (b1) < r (b2) < r (b3), VR_o (b1) > VR_o (b2) > VR_o (b3), Eq-R_o = 1.23).

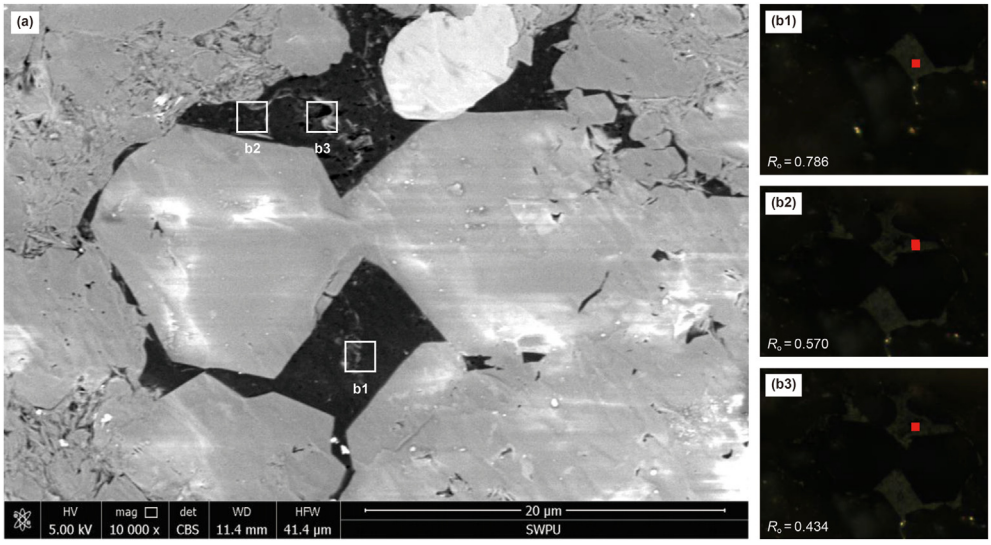

Fig. 15. Reflectance test values of solid bitumen at different pore development locations. (PA (b1) < PA (b2) < PA (b3), BR_o (b1) > BR_o (b2) > BR_o (b3), Eq-R_o = 0.98).

mentioned above also shows that the content of liptinite in Chang 7 shales is low, ranging from 4.8% to 14.3% (Fig. 5). Therefore, the contribution of liptinite to organic pores in chang 7 shale is minimal. On the other hand, the absence of pores in liptinite also indicates that it lacks primary pores. As for secondary pores, resinite enters the oil generation threshold earlier (0.35%R_o) (Snowdon and Powell, 1982; Khorasani and Michelsen, 1991), sporinite and cutinite enter moderately (0.5%R_o) (Brooks, 1970), and alginite enters later (0.6%R_o ~ 0.7%R_o) (Tissot and Welte, 1978). The maturity of Chang 7 shales ranges from 0.71% to 1.23%, which means that all kinds of liptinite have entered the stage of oil generation, but not yet entered the stage of abundant gas generation. Therefore, the secondary pores are not well developed. However, as a structure-altered maceral, liptinite can extensively develop hydrocarbon-bubble pores (the most common secondary pores) in post-mature marine shales (Yang et al., 2016a).

5.1.1.3. Vitrinite. The pore development characteristics of vitrinite under SEM are shown in Fig. 19. A certain amount of microcracks and pores can be found in vitrinite. The microcracks developed internally are hundreds of nanometers in width and tens of micrometers in length (Fig. 19a–c). The pores are mostly hydrocarbon-bubble pores and distributed sporadically (Fig. 19d). With round or elliptical pore morphology and the size of mesopores to macropores. Guo et al. (2018) also found cracks in the vitrinite of Chang 7 shale, which was explained as the fracture of vitrinite caused by compaction. Nevertheless, Yang et al. (2016a) regarded the crack developed in vitrinite as a hydrocarbon-shrinkage crack caused by the volumetric contraction of vitrinite. As for the pores in vitrinite, they are usually rarely found, whether in shales (Yang et al., 2019; Jia et al., 2021) or in coals (Everson et al., 2008; Giffin et al., 2013; Zhao et al., 2014; Cardott and Curtis, 2018). However, different types of pores (e.g. blowholes, breccia pores and broken pores) can still be observed in vitrinite of the anthracite of Lopingian (Shan et al., 2018). Furthermore, a smaller average nanopore diameter in vitrinte will influence its micro-mechanical properties,

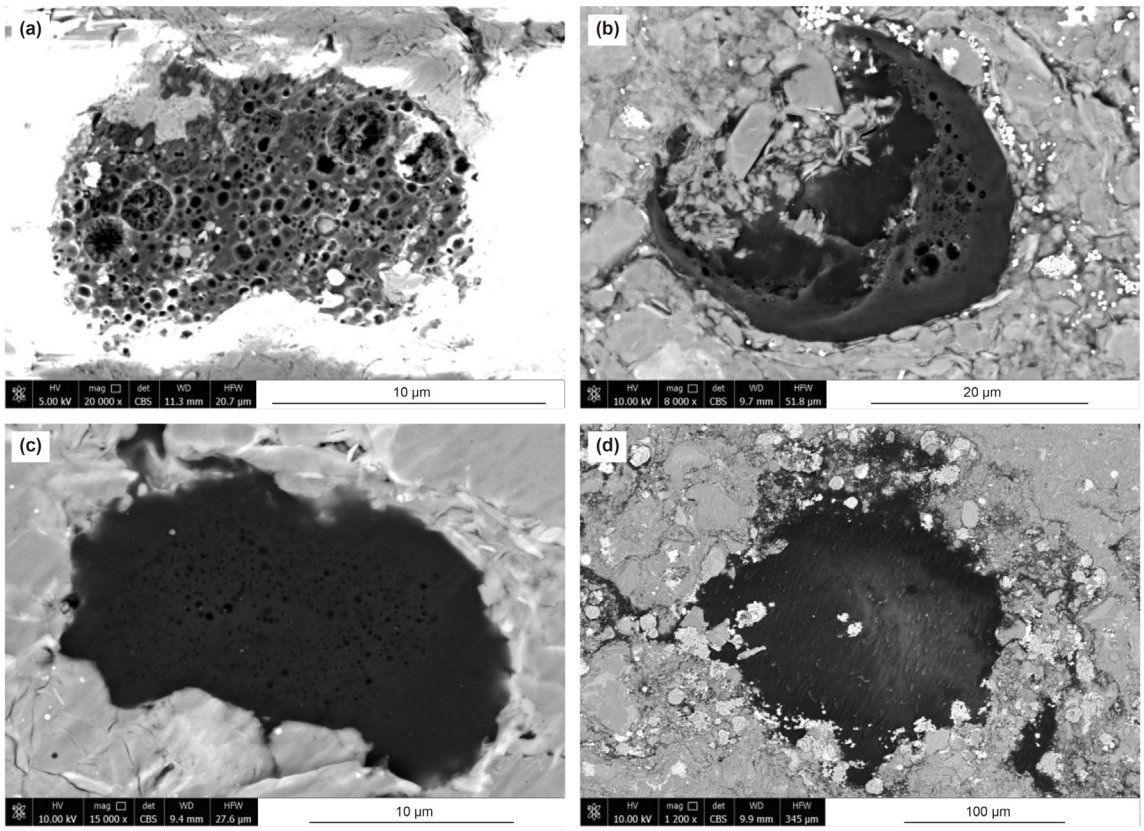

Fig. 16. Pores within alginite under SEM. (a, Yan56–2996.5; b, d, Zheng3-866.74; c, Zhuang233–1798.7).

because more efficient load distribution and resulting greater deformation resistiance can cause the decrease of the modulus (Vranjes-Wessely et al., 2020).

5.1.1.4. Inertinite. The pore development characteristics of inertinite under SEM can be seen in Fig. 20. The composition of inertinite in Chang 7 shales mainly includes fusinites and semifusinites. As the most well-preserved macerals of plant cells, fusinite developed significant primary pores that retain biological structure, which have irregular or elliptical pore shapes and pore sizes ranging from several microns to ten microns, such as plant cell lumens (Fig. 20a and b). At the same time, a certain amount of secondary pores generated in the process of hydrocarbon generation also exist in inertinite, which are mostly hundreds of nanometers in diameter and distributed in a dispersed manner (Fig. 20c–e). In addition, there are a small number of semifusinites without pores (Fig. 20f). So far, the pores of inertinite in shales and coal seams have been reported in many studies (Everson et al., 2008; Mastalerz et al., 2013; Coetzee et al., 2015; Yang et al., 2017; Jia et al., 2021; Lin et al., 2021). Similarly, Curtis et al. (2012) also proved the existence of primary fibroite (e.g., plant cell lumens) in Woodford Shale, a marine formation. Moreover, Shan et al. (2018) reported that, in the anthracite of Lopingian, the primary pores of plant tissue pores are prevalent in inertinite and rare in vitrinite. And secondary pores such as blowholes and cracks are more easily observed in vitrinite than inertinite. Similar conclusions were also reported in Jing et al. (2021), the pore structure of vitrinite and inertinite has obvious difference in the Permian coal from the Bowen Basin, Australia. Inertinite-rich sample has more pores, higher mesopore content and better connectivity than vitrinite-rich sample. These phenomena are highly consistent with our observations. In terms of pore size, inertinites contain more macropores (30 nm–10 μm in diameter) and less micropores (<2 nm) than vitrinites (Unsworth et al., 1989). As for the pore morphology in inertinite, it is controlled by the subclass of macerals. The pores in fusinite are large and elongated, while the morphology of macrinite pores is comparatively smaller and rounder (Giffin et al., 2013). In type II and type III kerogens rich in vitrinite and inertinite, the pores in organic matter particles are particularly enriched, and the micropore volume of OM is the largest, which has a good linear correlation with maturity (Chalmers and Bustin, 2007, 2008).

5.1.1.5. Solid bitumen. The pore development characteristics of solid bitumen under SEM are shown in Fig. 21. The pores in solid bitumen were densely distributed with an angular pore shape and pore sizes ranging from tens of nanometers to hundreds of nanometers. Some micro-cracks developed at the edge of solid bitumen and inorganic minerals or in solid bitumen. The width of the cracks is hundreds of nanometers, and the length can exceed 10 μm (Fig. 21f). At present, amounts of nanoscale pores have been also found in the solid bitumen of marine shales with high maturity and coal seams (Loucks et al., 2009; Mastalerz et al., 2013; Cardott and Curtis, 2018; Ma et al., 2020; Yao et al., 2021). Cao et al. (2020b) found that spongy pores are pervasion in solid bitumen of the Wufeng-Longmaxi shales in Guizhou, China, whose diameters span from nanometers to micrometers. Similarly, Hu et al. (2020) reported that solid bitumen is a porous component in the Longmaxi shales and amounts of sponge-like pores with diameter range of 8.4–1392.6 nm can be observed in solid bitumen under SEM. Even,

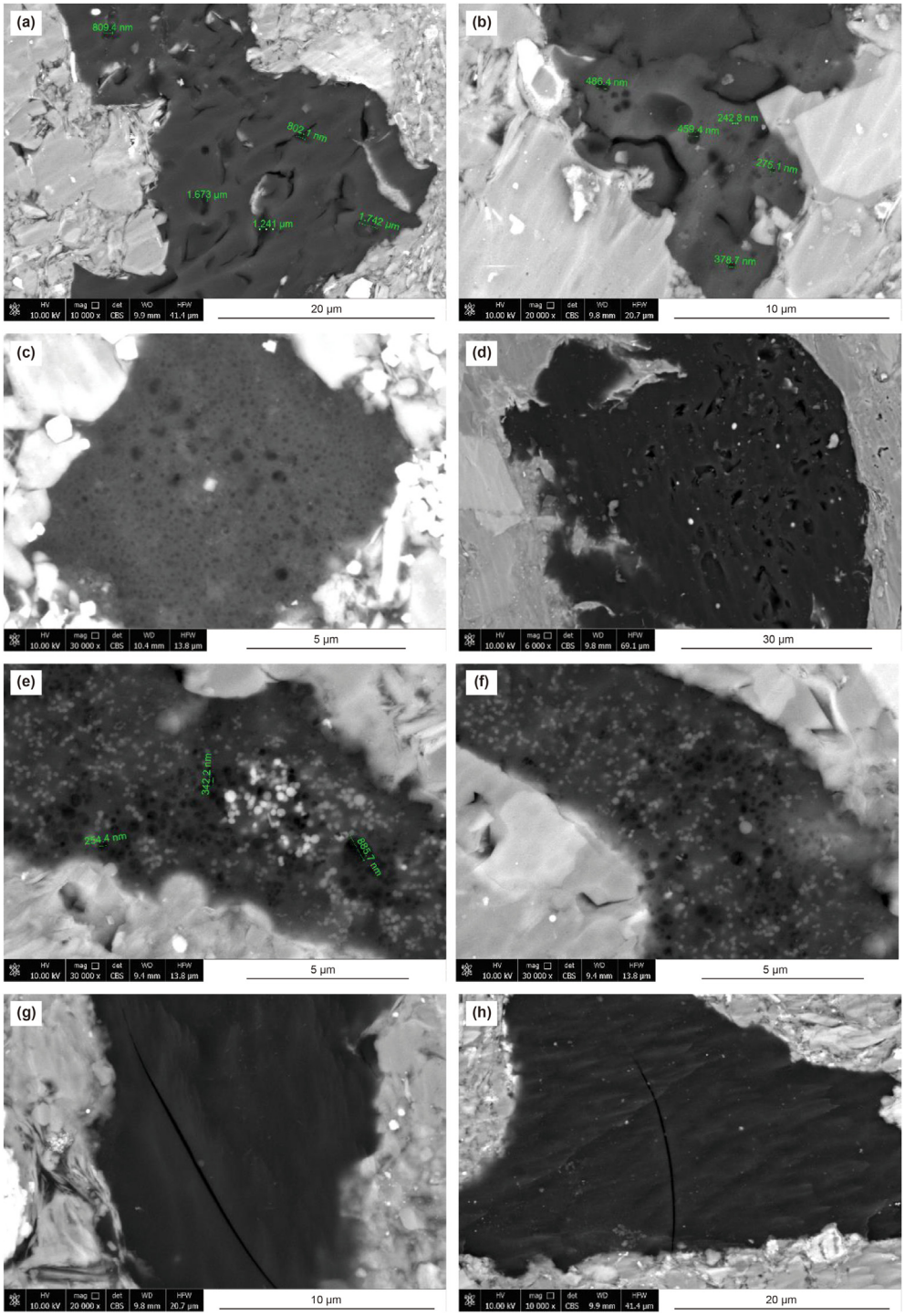

Fig. 17. Pores within bituminite under SEM. (a, b, Yan56–2978.5; c, Zhuang233-1790; d, Honghe21–1676.69; e, f, Zhuang233–1798.7; g, Huan317–2474.3; h, Yan56–2963.1).

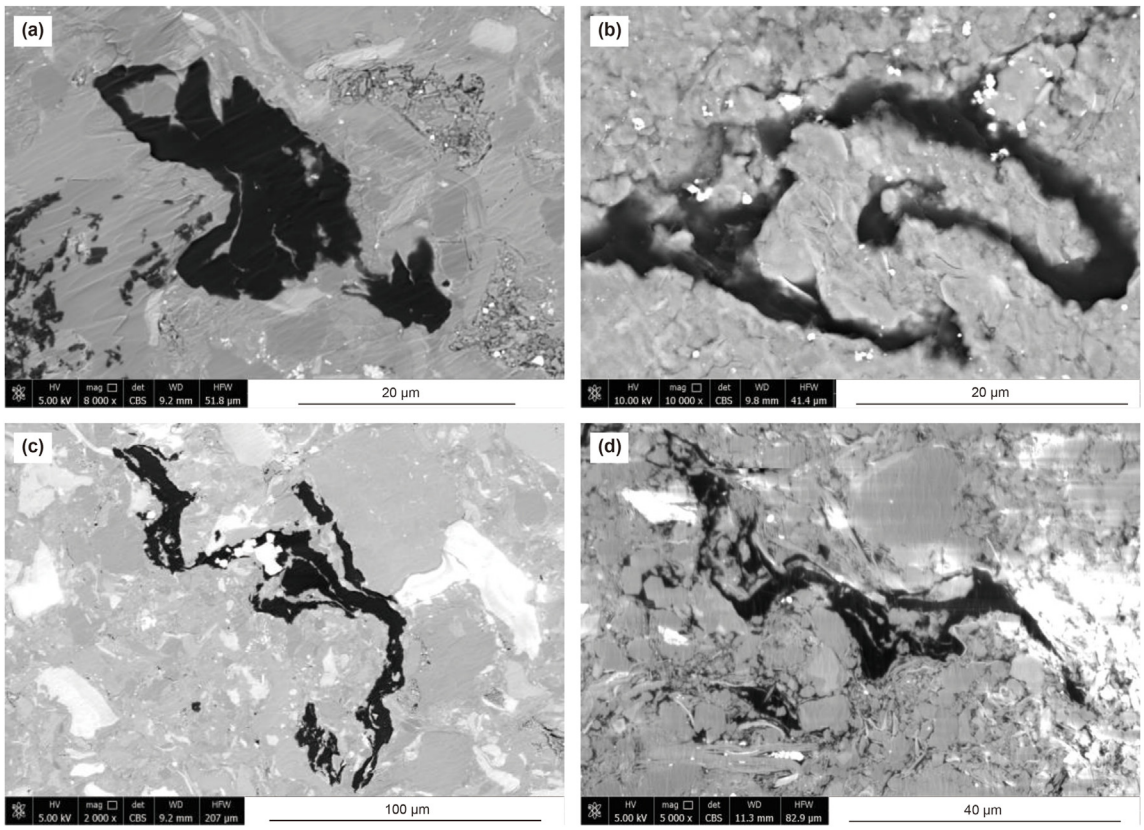

Fig. 18. Liptinite without visible pores under SEM. (a, Honghe21–1676.69, sporinite; b, Zheng3-866.74, sporinite; c, Honghe21–1676.69, cutinite; d, Huan317–2474.3, cutinite).

pores with various forms (such as pendular pores, spongy pores and interface pores) were found in solid bitumen from many strata, including Cambrian, Ordovician, Silurian, Upper Visean and Triassic (Misch et al., 2019). With regard to organic pores in solid bitumen, some researchers believe that the main mechanism of its formation is that the gas generated by bitumen cracking cannot be effectively discharged (Chalmers and Bustin, 2017). As mentioned by Piane et al. (2018), solid bitumen was originally infiltrated into mineral pore space as a liquid phase, which led to the formation of an organic network. With the increase of maturity, gaseous hydrocarbons were generated from solid bitumen during secondary thermal cracking process, resulting in the formation of organic pores.

5.1.2. Quantitative characterization

The characterization of PSDs of different macerals in Chang 7 shales are shown in Fig. 22. The main peaks of PSDs of alginite and bituminite were in the range of 100–200 nm (Fig. 22a and b), with average pore sizes of 316.56 nm and 418.86 nm, respectively (Table 7). The pore diameters of spoinites, cutinites and resinite are relatively large, mostly in the range of 300–700 nm (Fig. 22c–e), with average pore sizes of 800.94 nm, 419.69 nm and 751.01 nm, respectively. Vitrinite and fusinite have a wide PSD, with a certain amount of organic pores ranging from 0 nm to 2500 nm, and the average pore sizes are 601.95 nm and 643.85 nm, respectively. And the main peak range of their PSDs is 200–300 nm (Fig. 22f and g). As for solid bitumen, its PSD is quite concentrated, mainly distributed in the range of 0–200 nm, and the average pore size is 215.57 nm. The pores in other diameter scales are less developed (Fig. 22h). Therefore, according to the main peak range of PSDs of various macerals, the order of organic pore diameter from small to large is solid bitumen, bituminite, alginite, vitrinite, fusinite and liptinite. Hu et al. (2017) reported that organic pore diameter was varied in the range of 5–1021 nm and averaged 68 nm in the Wufeng-Longmaxi shale. Wang et al. (2020) reported that the main range of organic matter pore size distribution is 100–200 nm in the Longmaxi shale. In addition, similar PSD patterns of organic pores have been found in many studies (Hu et al., 2017; Guan et al., 2019). All these researches focus on describing the PSD of organic pores as a whole, but ignore the PSD of organic pores derived from various macerals.

Plane porosity of macerals for studied samples was shown in Table 8 and Fig. 23. The plane porosity of organic pores in alginite and bituminite were in the ranges of 7.23%–20.74% and 3.19%–26.70%, with an average of 16.03% and 11.09%, respectively. The sporinites, cutinites and resinites in liptinite are not only low in content, but also have very poor development of organic pores, with an average plane porosity of only about 2%. The plane porosity of vitrinite ranges from 0.65% to 3.54% and averages 2.13%. And, the plane porosity of fusinite and solid bitumen were in the ranges of 1.68%–25.61% and 1.91%–21.56%, with an average of 12.05% and 7.98%, respectively. It can be found that the quantitative calculation results are consistent with the organic pore development characteristics of each macerals observed qualitatively by FE-SEM. The average plane porosity was used to evaluate the development degree of OM pores in macerals, and the order from high to low was alginite, fusinite, bituminite, solid bitumen, vitrinite and liptinite. Among them, alginite, fusinite and bituminite have certain primary pores, while solid bitumen only produces secondary pores. Hu et al. (2020) reported similar results in the overmature shales of Longmaxi Formation. The plane porosities of alginite and solid bitumen range from 11.1% to 16.7% and 11.6%–14.7%, respectively.

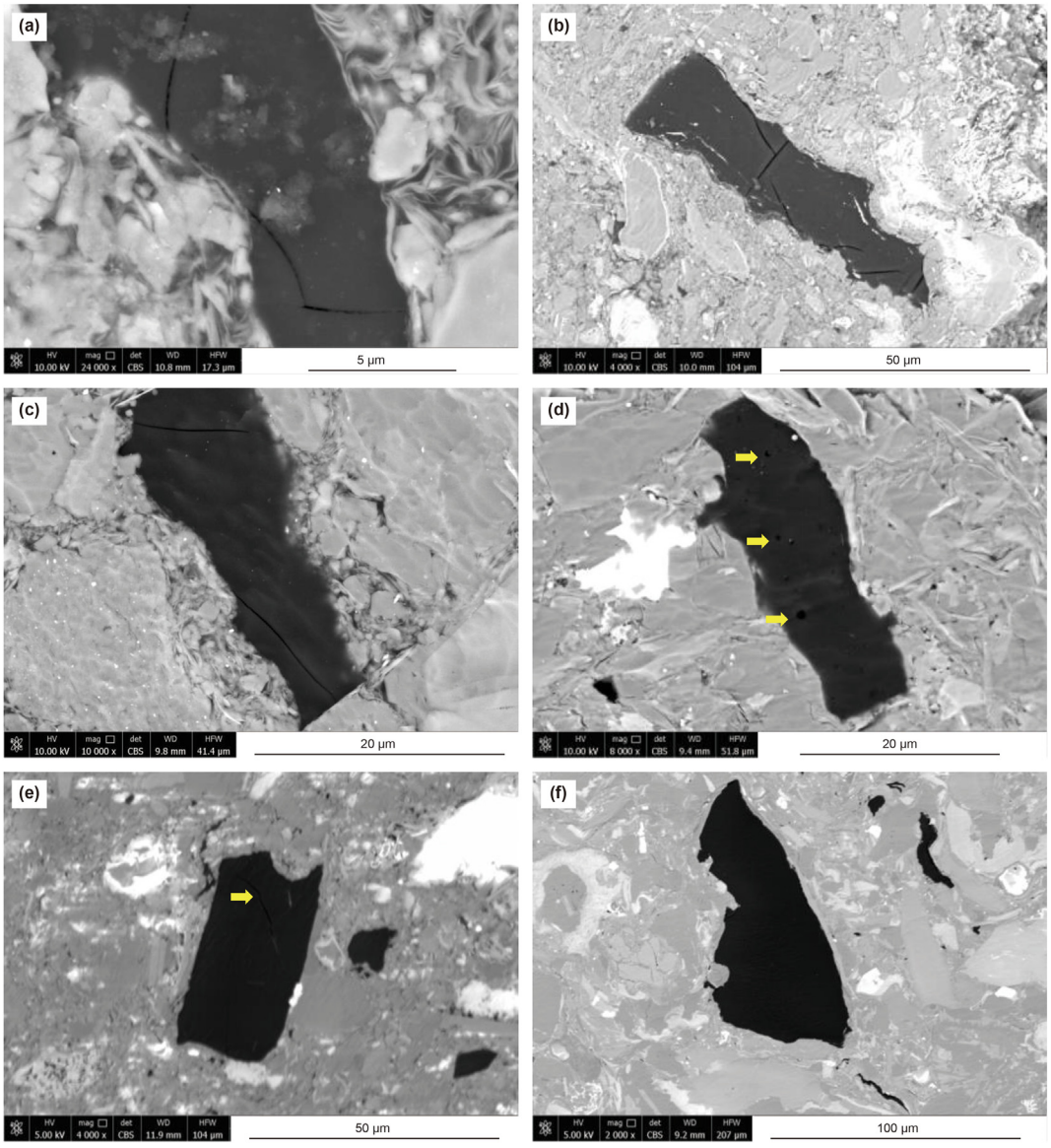

Fig. 19. Cracks and pores within vitrinite under SEM. (a, Huan317–2468.3; b, Yan56–2978.5; c, Huan317–2474.3; d, Zhuang233–1798.7; e, Yan56–2963.1; f, Honghe21–1676.69).

Meanwhile, Loucks et al. (2009) and Misch et al. (2019) have also observed a mass of primary pores in alginite whose morphology is consistent with biological structure. As for solid bitumen, the random occurrence of secondary gas-generated pores with a sponge-like pattern is the most prevalent in it. Different from the typical marine shale, the pores of solid bitumen in Longmaxi shales have larger diameters and higher abundance than those in bituminite (Cao et al., 2020b; Hu et al., 2020). However, in our study, the size and abundance of solid bitumen pores are lower than those of bituminite in Chang 7 shales, which is attributed to the low maturity ($0.71\% \leq$ Eq-$R_o \leq 1.23\%$) of Chang 7 shale. At this stage, the development of organic pore in solid bitumen is limited due to the lack of gaseous hydrocarbons generation.

In addition, the relative contributions of macerals to organic pores were calculated using Eq. (2).

$$C_{\text{macerals}} = (PA_{\text{macerals}}/PA_{\text{OM}}) \times 100 \quad (2)$$

where C_{macerals} is the relative contribution (%) of macerals to organic pores, PA_{macerals} is the pore area (m^2) of macerals, PA_{OM} represents total pore area (m^2) of all OM. The calculated relative contributions of macerals to the organic pore area were shown in Table 9 and Fig. 24. The relative contribution of alginite and bituminite to organic pores varies from 2.93% to 59.44% and 18.29%–91.36%, with an average value of 36.97% and 56.62%, respectively. The contributions of sporinite, cutinite and resinite to organic pores are quite low, with an average contribution of only about 4%. The relative contribution of vitrinite, fusinite and solid bitumen to organic pores vary in the ranges of 0.05%–3.77%, 1.86%–48.61% and 1.20%–33.83%, respectively. From Fig. 24, it can be found that bituminite contributes the most to the pores of OM, followed by solid bitumen and fusinite. Current research almost focuses on the relative contribution of inorganic minerals and organic matter to shale pore volume (e.g. Han et al., 2019; Chen et al., 2021; Gao et al., 2021). However, the relative quantitative contributions of various macerals in OM to organic pores has not been reported in detail.

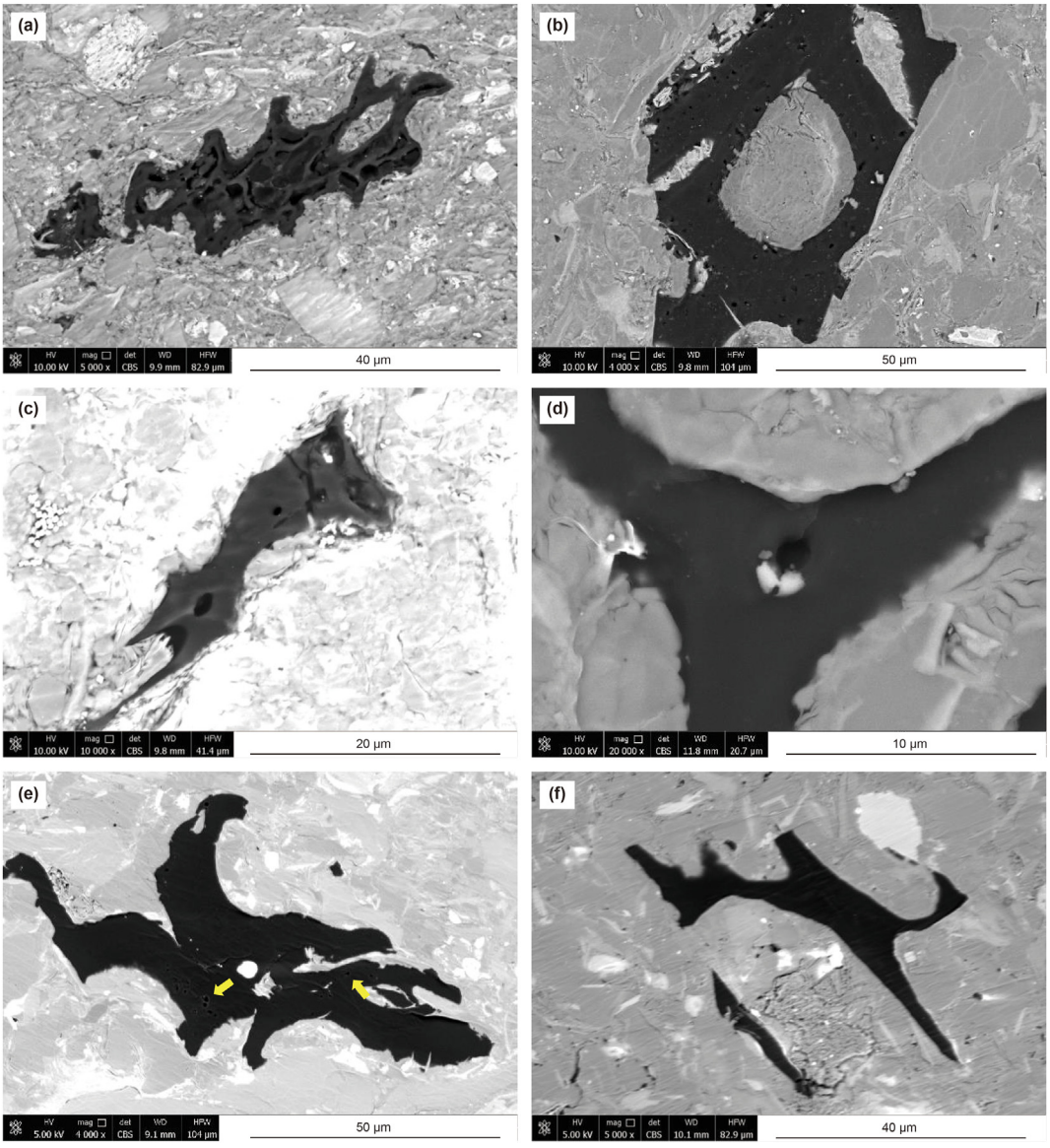

Fig. 20. Pores within inertinite under SEM. (a, Yan56–2963.1; b, e, Honghe21–1676.69; c, Zheng3-866.74; d, Jinghe13–1357.23; f, Zhuang233–1798.7).

5.2. Influence of maturity on pore structure

To analyze the thermal evolution characteristics of organic pores of prevalent macerals in Chang 7 shales, the relationship between plane porosity and equivalent vitrinite reflectance (Eq-R_o) was analyzed in Fig. 25. There is a certain positive correlation between the plane porostiy and Eq-R_o of the bituminite (Fig. 25a), suggesting that the pores of bituminite become more enriched with the process of hydrocarbon generation and expulsion during thermal evolution. In the thermal evolution process, the plane porosity of fusinite is mainly distributed in the range of 20%–28% and 1%–7% (Fig. 25c). Based on the cognition of SEM observation, it is speculated that the former is dominated by relatively developed primary cellular lumen pores (Fig. 20a and b), while the latter mainly represents secondary pores formed in the process of hydrocarbon generation during thermal evolution (Fig. 20c–e). At the same time, a certain positive correlation between plane porosity and vitrinite reflectance in the latter also verifies this conjecture. As for the organic pores of vitrinite and solid bitumen, no obvious thermal evolution law was found (Fig. 25b, d). At first, most scholars believed that as the organic matter was thermally decomposed to generate and discharge hydrocarbons, the decomposed part would form pores (Jarvie et al., 2007; Chalmers and Bustin, 2008; Sisk et al., 2010; Bernard et al., 2012; Pommer and Milliken, 2015). Therefore, the development degree of OM pores should increase with the increase of hydrocarbon conversion rate. Some scholars have established the prediction model of organic pore development according to the theory of hydrocarbon generation kinetics (Modica and Lapierre, 2012; Romero-Sarmiento et al., 2013; Chen and Jiang, 2016). However, the experimental results show that the development degree of organic pores does not increase linearly with the increase of maturity. For example, Curtis et al. (2012), when studying the variation of OM pores in Woodford shale with thermal evolution, found that there were almost no organic pores in shale samples when R_o was less than 0.9%, organic pores showed an irregular change when R_o was between 1.23% and 2.0%, and no OM pores were observed when R_o was more than 2.0%. Fishman et al. (2012) also found that there was no significant relationship

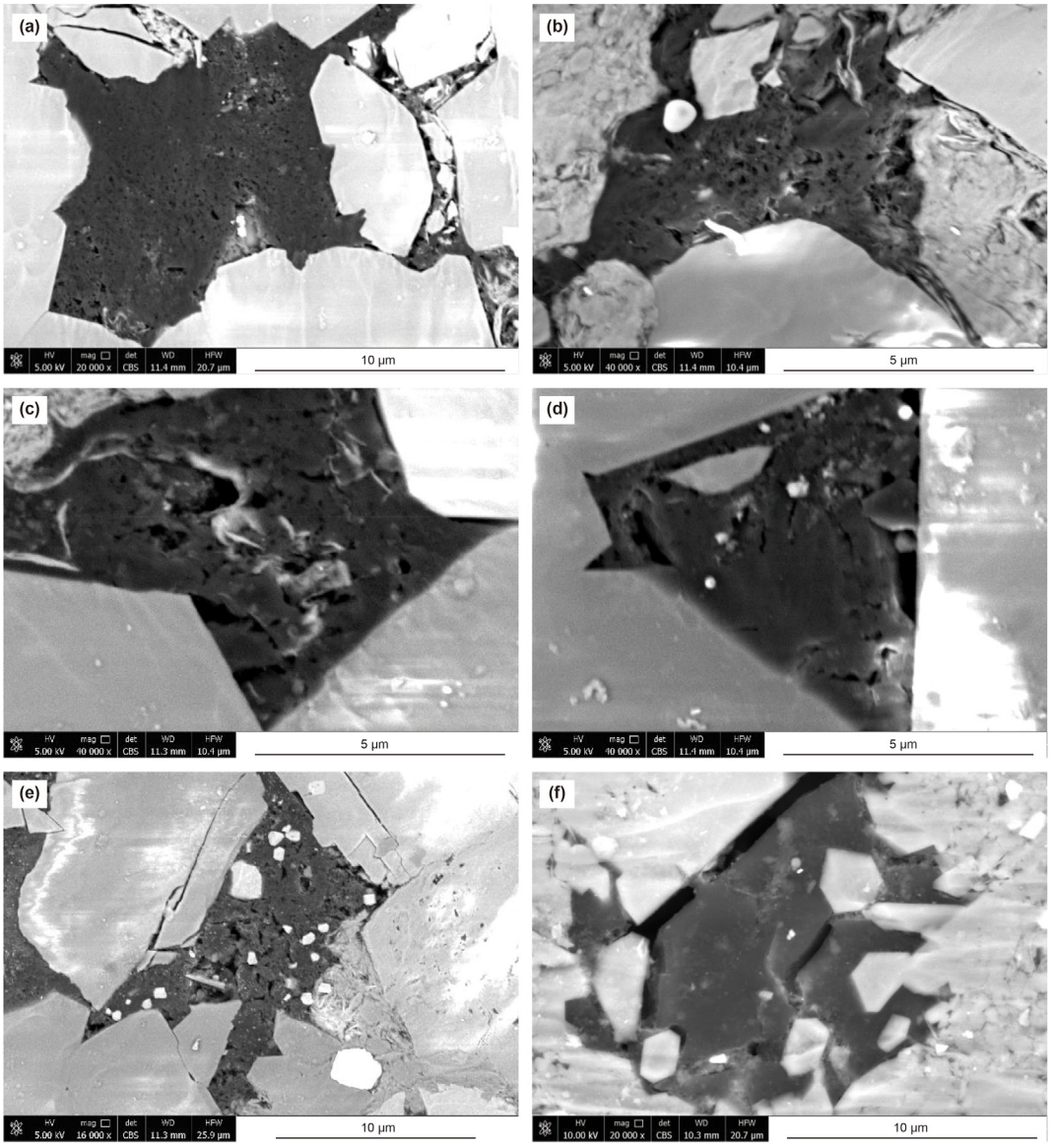

Fig. 21. Well-developed pores within solid bitumen under SEM (a-e, Yan56–2996.5; f, Zhuang233-1790).

between organic pore development and thermal evolution in organic-rich mudstones of the Upper Jurassic Kimmeridge Clay Formation, North Sea. In general, although thermal evolution has an important effect on the formation of organic pores, there is no clear linear relationship between organic pore development and maturity. Our results also show that thermal maturity is not the only factor controlling the development of OM pores, and maceral type has a significant influence on the formation of OM pores, too.

5.3. Comparsion between the results of FE-SEM and LPGA

Since the characterization range of LPGA is 0–200 nm, its results can be used to verify the characterization effect of SEM in the smaller nanometer range. Taking into account the 5 nm resolution of SEM (Chalmers et al., 2012), the characterization results derived from FE-SEM and LPGA with the range of 5–200 nm were compared in our study. It can be found that with the increase of pore structure parameters (pore volume and surface area) calculated by LPGA, the plane porosity characterized by SEM always maintained a low value (Fig. 26). This confirms that the organic pores distributed in the range of 5–200 nm cannot be fully identified by SEM. Therefore, the combination of iCLEM and LPGA to characterize organic pores is recommended in our study. At present, the combined use of SEM and gas adsorption to characterize nanoscale pore structure has been reported in some literatures (Yang et al., 2016b; Wang et al., 2017, 2021; Zhou et al., 2018; Gou et al., 2019; Liu et al., 2019; Zhang et al., 2020b; Han et al., 2022). However, the combination of iCLEM and gas adsorption to characterize the pores in macerals has yet to be popularized.

5.4. Effect of pore structure on reflectance

Vitrinite reflectance was considered as the most reliable parameter reflecting the thermal evolution degree of sedimentary

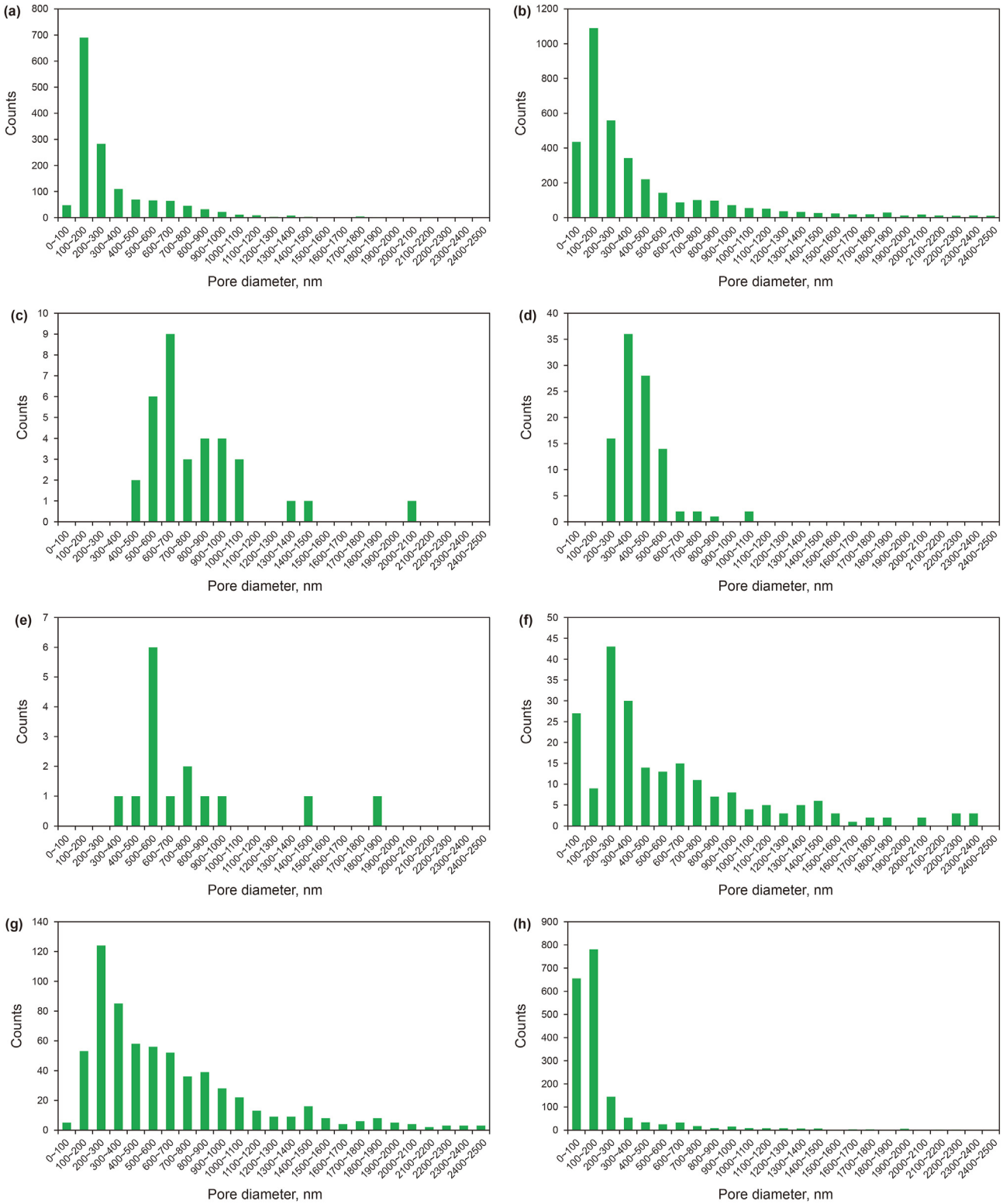

Fig. 22. PSDs of organic pores of different macerals. (a: Alginite; b: Bituminite; c: Sporinite; d: Cutinite; e: Resinite; f: Vitrinite; g: Fusinite; h: Solid bitumen).

Table 7
Statistical results of organic pores of macerals.

OM types	Total pore counts	Minimum pore diameter (nm)	Maximum pore diameter (nm)	Average pore diameter (nm)
Alginite	1473	53.7	2272	316.56
Bituminite	3509	37.5	2493	418.86
Sporinite	34	416	2014	800.94
Cutinite	101	228	1063	419.69
Resinite	15	386	1835	751.01
Vitrinite	216	37.4	2396	601.95
Fusinite	651	79.2	2473	643.85
Solid bitumen	1835	32.7	2481	215.57

Table 8
Plane porosity of organic pores of macerals for Chang 7 shale samples.

Sample	Alginite (%)	Bituminite (%)	Sporinite (%)	Cutinite (%)	Resinite (%)	Vitrinite (%)	Fusinite (%)	Solid bitumen (%)
1	20.12	23.64				3.09	20.79	
2	7.23	4.71				2.09		3.65
3		6.44					2.59	11.40
4		10.98	1.70		2.68	0.65	1.86	2.94
5		3.19		2.76			1.68	
6		7.29				1.19	25.61	21.56
7		9.59	1.82			3.54	4.83	6.84
8	20.74	7.61				2.95	22.02	7.57
9		10.74			1.43	1.64	23.97	
10		26.70				1.91	5.05	1.91
Average value	16.03	11.09	1.76	2.76	2.05	2.13	12.05	7.98

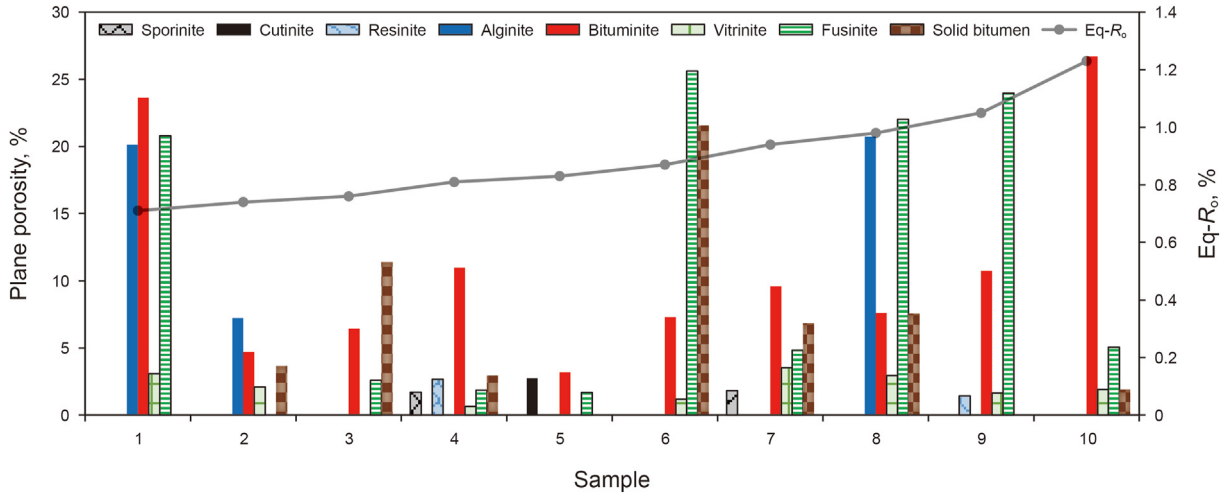

Fig. 23. Plane porosity of organic pores of macerals for studied samples.

Table 9
Relative contributions of macerals to OM area of the studied samples.

Sample	Alginite (%)	Bituminite (%)	Sporinite (%)	Cutinite (%)	Resinite (%)	Vitrinite (%)	Fusinite (%)	Solid bitumen (%)
1	2.93	54.97				0.47	41.64	
2	59.44	18.29				2.65		19.63
3		63.65					2.52	33.83
4		67.54	7.49		6.66	1.89	1.86	14.58
5		64.18		4.50			31.31	
6		47.26				2.56	48.61	1.57
7		80.80	0.36			3.64	8.46	6.74
8	48.55	25.94				0.05	15.10	10.36
9		52.23			0.67	3.77	43.33	
10		91.36				2.94	4.51	1.20
Average value	36.97	56.62	3.92	4.50	3.66	2.25	21.93	12.56

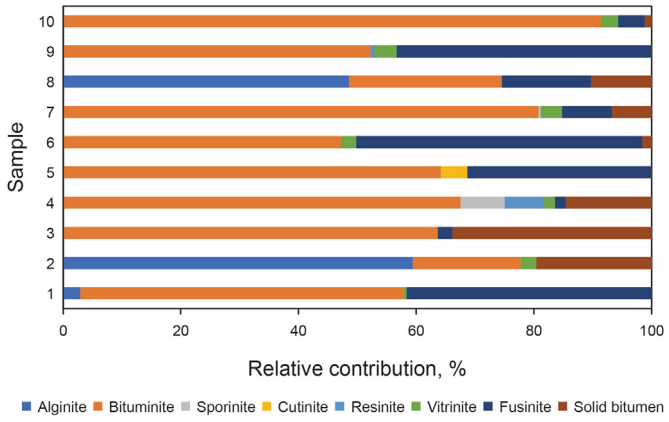

Fig. 24. Relative contributions of macerals to OM pores of the studied samples.

organic matter (Taylor et al., 1998; Corcoran and Doré, 2005; Dembicki, 2009; Suárez-Ruiz et al., 2012). The plane porosity at each test point in vitrinite and solid bitumen was calculated using JMicroVision and listed in Table 10, and the relationship between plane porosity and reflectance measurements was plotted in Fig. 27. It can be seen that in the same piece of organic matter (vitrinite or solid bitumen), the plane porosity of organic pores has a good negative correlation with the measured value of reflectance. Moreover, the effect of organic pores on vitrinite reflectance is greater than that of solid bitumen (Fig. 27), which may be related to the more homogeneous and smooth surface structure of vitrinite compared with solid bitumen. Because the surface which was originally more homogeneous and smoother has a more obvious contrast of roughness after the formation of organic pores. Some studies have found that the reflectance of vitrinite with a rougher surface in the same sample is lower than that of vitrinite with a smoother surface (Borrego et al., 2006; Grobe et al., 2017), and the reflectance of solid bitumen is similarly affected (Sanei et al., 2015, 2016; Mastalerz and Schieber, 2017; Valentine et al., 2019). The development of OM pores is bound to affect the surface roughness of vitrinite and solid bitumen. The larger the pore size and the more developed the pores, the rougher the surface of vitrinite and solid bitumen, resulting in a lower reflectance value. Based on this effect, when measuring the reflectivity of vitrinite and solid bitumen, the measurement point should be as small as possible and the test place should be selected where the pores are not developed, so as to avoid the influence of organic pores on the test results.

6. Conclusions

To quantitatively evaluate the pore characteristics of various macerals in Chang 7 lacustrine shales, iCLEM and LPGA were performed on macerals and organic matter samples, respectively. And the relative contributions of macerals to organic pores were estimated. On the basis of the geochemical parameters, the thermal evolution law of organic pores in macerals was analyzed. Finally, the influence of organic pores on reflectance of vitrinite and solid bitumen was discussed by performing reflectance measurement experiment. Main conclusions of this research are as follows.

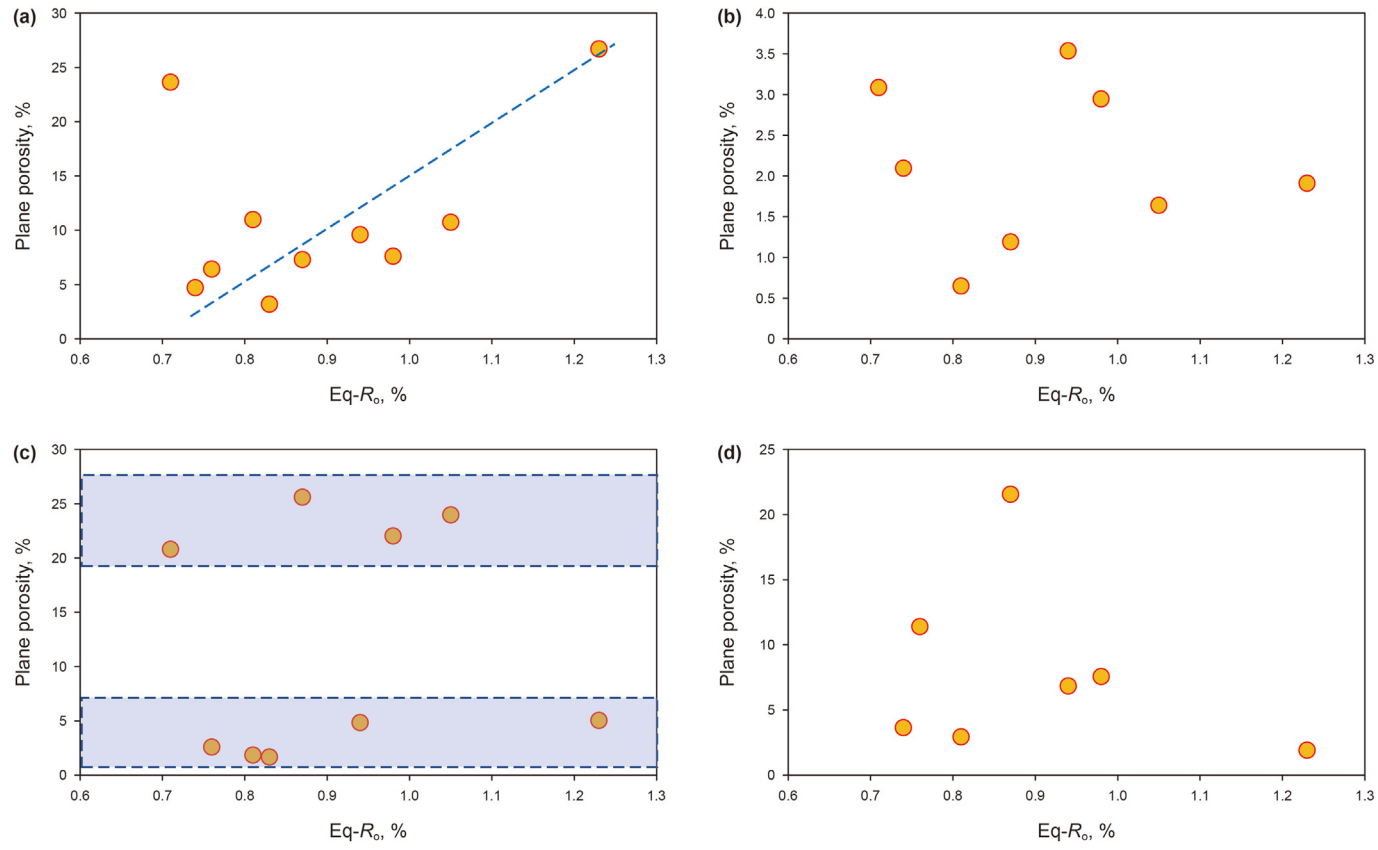

Fig. 25. Relationship between plane porosity and maturity of pores in common macerals. (a: Bituminite; b: Vitrinite; c: Fusinite; d: Solid bitumen).

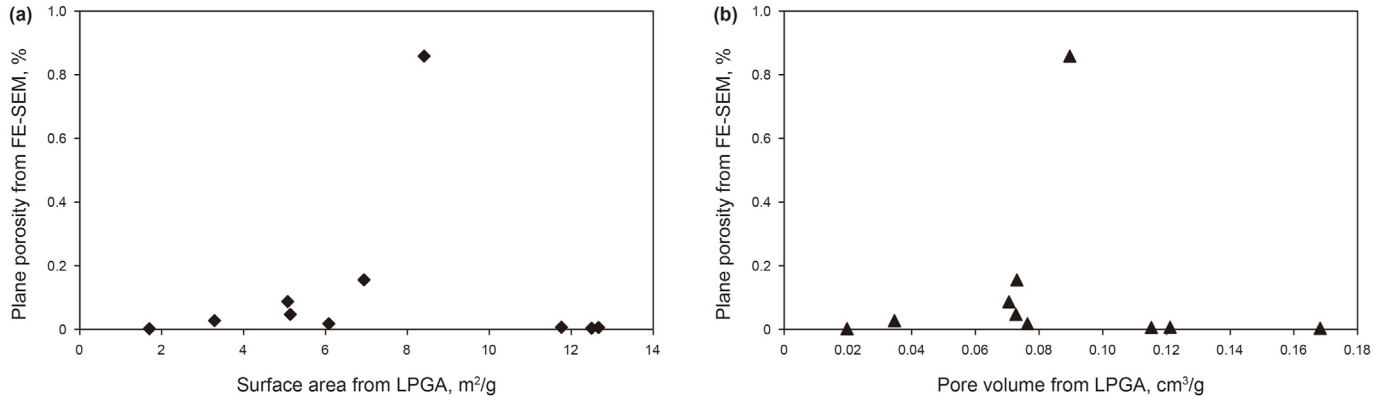

Fig. 26. Correlation diagram of pore structure parameters from FE-SEM and LPGA in the range of 5–200 nm.

Table 10
Reflectance and plane porosity at test points of vitrinite and solid bitumen.

Macerals	Plot	Plane porosity (%)	Reflectance (%)
Vitrinite	b1	1.16	1.484
	b2	7.86	1.176
	b3	13.79	0.92
Solid bitumen	b1	2.70	0.786
	b2	8.98	0.570
	b3	26.30	0.434

(1) The organic pores of Chang 7 shale are mostly circular or elliptical in morphology, usually aggregated in a honeycomb shape. The organic pores are mainly distributed in the range of 100–400 nm, and the average plane porosity of macerals is 10.13%.
(2) Among various macerals, sapropelinite preserved a certain amount of organic pores, but almost no pores existed in liptinite. There was a small amount of microcracks and pores in vitrinite, and a large number of primary pores that retained plant structure can be seen in fusinite. Due to the process of hydrocarbon generation and expulsion, solid bitumen formed amounts of organic pores and microcracks.
(3) The order of organic pore diameter from small to large is solid bitumen, bituminite, alginite, vitrinite, fusinite and liptinite, and the order of pore development degree from high to low was alginite, fusinite, bituminite, solid bitumen, vitrinite and liptinite. The contribution of organic pores mainly comes from bituminite, solid bitumen and fusinite. As for the controlling factors of organic pore development, thermal maturity is not the only factor, and maceral type also has a significant influence on the formation of organic pores.
(4) The development of organic pores (an increase in pore size and pore number) enhances the surface roughness of vitrinite or solid bitumen, resulting in an underestimate of their reflectances.

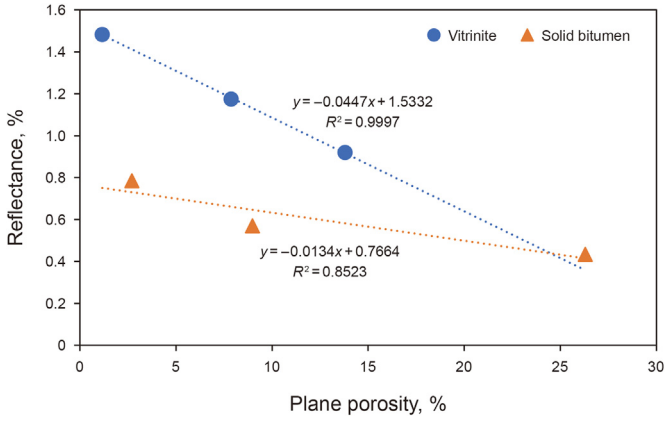

Fig. 27. Relationship between reflectance and plane porosity in vitrinite and solid bitumen.

Acknowledgements

This project was funded by the National Natural Science Foundation of China (41972161), the 2021 American Association of Petroleum Geologists Foundation Grants-in-Aid Program and Science and Technology Cooperation Project of the CNPC-SWPU Innovation Alliance (2020CX050103).

References

Ardakani, O.H., Sanei, H., Ghanizadeh, A., Lavoie, D., Chen, Z., Clarkson, C.R., 2018. Do all fractions of organic matter contribute equally in shale porosity? A case study from Upper Ordovician Utica Shale, southern Quebec, Canada. Mar. Petrol. Geol. 92, 794–808. https://doi.org/10.1016/j.marpetgeo.2017.12.009.

Baruch, E.T., Kennedy, M.J., Löhr, S.C., Dewhurst, D.N., 2015. Feldspar dissolution-enhanced porosity in Paleoproterozoic shale reservoir facies from the Barney Creek Format ion (McArthur Basin, Australia). AAPG (Am. Assoc. Pet. Geol.) Bull. 99, 1745–1770. https://doi.org/10.1306/04061514181.

Bai, L.H., Liu, B., Du, Y.J., Wang, B.Y., Tian, S.S., Wang, L., Xue, Z.Q., 2022. Distribution characteristics and oil mobility thresholds in lacustrine shale reservoir: insights from N2 adsorption experiments on samples prior to and following hydrocarbon extraction. Petrol. Sci. 19 (2), 486–497. https://doi.org/10.1016/j.petsci.2021.10.018.

Bernard, S., Horsfield, B., Schulz, H.M., Wirth, R., Schreiber, A., Sherwood, N., 2012. Geochemical evolution of organic-rich shales with increasing maturity: a STXM and TEM study of the Posidonia Shale (Lower Toarcian, northern Germany). Mar. Petrol. Geol. 31, 70–89. https://doi.org/10.1016/j.marpetgeo.2011.05.010.

Borjigin, T., Lu, L.F., Yu, L.J., Zhang, W.T., Anyang, P.A.N., Gao, Z.W., 2021. Formation, preservation and connectivity control of organic pores in shale. Petrol. Explor. Dev. 48 (4), 798–812. https://doi.org/10.1016/S1876-3804(21)60067-8.

Borrego, A.G., Araujo, C.V., Balke, A., Cardott, B., Cook, A.C., David, P., Vieth, A., 2006. Influence of particle and surface quality on the vitrinite reflectance of dispersed organic matter: comparative exercise using data from the qualifying system for reflectance analysis working group of ICCP. Int. J. Coal Geol. 68, 151–170. https://doi.org/10.1016/j.coal.2006.02.002.

Bostick, N., Alpern, B., 1977. Principles of sampling, preparation and constituent selection for microphotometry in measurement of maturation of sedimentary organic matter. J. Microsc. 109, 41–47. https://doi.org/10.1111/j.1365-2818.1977.tb01115.x.

Brooks, J., 1970. The use of coals as indicators of the occurrence of oil and gas. The APPEA Journal 10, 35–40. https://doi.org/10.1071/AJ69007.

Brunauer, S., Deming, L.S., Deming, W.E., Teller, E., 1940. On a theory of the van der Waals adsorption of gases. J. Am. Chem. Soc. 62, 1723–1732. https://doi.org/10.1021/ja01864a025.

Bustin, R.M., Bustin, A.M., Cui, A., Ross, D., Pathi, V.M., 2008. Impact of shale

properties on pore structure and storage characteristics. In: SPE Shale Gas Production Conference, Fort Worth, Texas, USA, pp. 16–18. https://doi.org/10.2118/119892-MS. Novermber, SPE Paper 119892.
Cao, T., Xu, H., Liu, G., Deng, M., Cao, Q., Yu, Y., 2020b. Factors influencing microstructure and porosity in shales of the Wufeng-Longmaxi formations in northwestern Guizhou, China. J. Petrol. Sci. Eng. 191, 107181. https://doi.org/10.1016/j.petrol.2020.107181.
Cao, Y., Han, H., Guo, C., Pang, P., Ding, Z.G., Gao, Y., 2020a. Influence of extractable organic matters on pore structure and its evolution of Chang 7 member shales in the Ordos Basin, China: implications from extractions using various solvents. J. Nat. Gas Sci. Eng. 79, 103370. https://doi.org/10.1016/j.jngse.2020.103370.
Cao, Y., Han, H., Liu, H.W., Jia, J.C., Zhang, W., Liu, P.W., Gao, Y., 2019. Influence of solvents on pore structure and methane adsorption capacity of lacustrine shales: an example from a Chang 7 shale sample in the Ordos Basin, China. J. Petrol. Sci. Eng. 178, 419–428. https://doi.org/10.1016/j.petrol.2019.03.052.
Cao, Z., Liu, G., Zhan, H., Li, C., You, Y., Yang, C., Jiang, H., 2016. Pore structure characterization of Chang-7 tight sandstone using MICP combined with N_2GA techniques and its geological control factors. Sci. Rep. 6, 1–13. https://doi.org/10.1038/srep36919.
Cardott, B.J., Curtis, M.E., 2018. Identification and nanoporosity of macerals in coal by scanning electron microscopy. Int. J. Coal Geol. 190, 205–217. https://doi.org/10.1016/j.coal.2017.07.003.
Cardott, B.J., Landis, C.R., Curtis, M.E., 2015. Post-oil solid bitumen network in the Woodford Shale, USA—a potential primary migration pathway. Int. J. Coal Geol. 139, 106–113. https://doi.org/10.1016/j.coal.2014.08.012.
Chalmers, G.R., Bustin, R.M., 2007. The organic matter distribution and methane capacity of the Lower Cretaceous strata of Northeastern British Columbia, Canada. Int. J. Coal Geol. 70, 223–239. https://doi.org/10.1016/j.coal.2006.05.001.
Chalmers, G.R., Bustin, R.M., 2008. Lower Cretaceous gas shales in northeastern British Columbia, Part I: geological controls on methane sorption capacity. Bull. Can. Petrol. Geol. 56, 1–21. https://doi.org/10.2113/gscpgbull.56.1.1.
Chalmers, G.R., Bustin, R.M., 2015. Porosity and pore size distribution of deeply-buried fine-grained rocks: influence of diagenetic and metamorphic processes on shale reservoir quality and exploration. Journal of Uncoventional Oil and Gas Resources 12, 134–142. https://doi.org/10.1016/j.juogr.2015.09.005.
Chalmers, G.R., Bustin, R.M., 2017. A multidisciplinary approach in determining the maceral (kerogen type) and mineralogical composition of Upper Cretaceous Eagle Ford Formation: impact on pore development and pore size distribution. Int. J. Coal Geol. 171, 93–110. https://doi.org/10.1016/j.coal.2017.01.004.
Chalmers, G.R., Bustin, R.M., Power, I.M., 2012. Characterization of gas shale pore systems by porosimetry, pycnometry, surface area, and field emission scanning electron microscopy/transmission electron microscopy image analyses: examples from the Barnett, Woodford, Haynesville, Marcellus, and Doig unitsCharacterization of Gas Shale Pore Systems. AAPG (Am. Assoc. Pet. Geol.) Bull. 96, 1099–1119. https://doi.org/10.1306/10171111052.
Chen, J., Jiang, F., Hu, T., Wang, Z., Xu, Z., Peng, J., Li, L., 2016. Experimental investigation of the characteristics of organic matter pores in Chang 7 member lacustrine shale from the Ordos Basin due to organic matter evolution induced by hydrous pyrolysis. J. Nat. Gas Sci. Eng. 35, 412–424. https://doi.org/10.1016/j.jngse.2016.08.069.
Chen, S., Li, X., Chen, S., Wang, Y., Gong, Z., Zhang, Y., 2021. A new application of atomic force microscopy in the characterization of pore structure and pore contribution in shale gas reservoirs. J. Nat. Gas Sci. Eng. 88, 103802. https://doi.org/10.1016/j.jngse.2021.103802.
Chen, Z., Jiang, C., 2016. A revised method for organic porosity estimation in shale reservoirs using Rock-Eval data: example from Duvernay Formation in the Western Canada Sedimentary Basin. AAPG (Am. Assoc. Pet. Geol.) Bull. 100, 405–422. https://doi.org/10.1306/08261514173.
Chen, Z., Song, Y., Jiang, Z., Liu, S., Li, Z., Shi, D., Guo, X., 2019. Identification of organic matter components and organic pore characteristics of marine shale: a case study of Wufeng-Longmaxi shale in southern Sichuan Basin, China. Mar. Petrol. Geol. 109, 56–69. https://doi.org/10.1016/j.marpetgeo.2019.06.002.
Coetzee, G.H., Sakurovs, R., Neomagus, H.W., Morpeth, L., Everson, R.C., Mathews, J.P., Bunt, J.R., 2015. Pore development during gasification of South African inertinite-rich chars evaluated using small angle X-ray scattering. Carbon 95, 250–260. https://doi.org/10.1016/j.carbon.2015.08.030.
Corcoran, D., Doré, A., 2005. A review of techniques for the estimation of magnitude and timing of exhumation in offshore basins. Earth Sci. Rev. 72, 129–168. https://doi.org/10.1016/j.earscirev.2005.05.003.
Curtis, J.B., 2002. Fractured shale-gas systems. AAPG (Am. Assoc. Pet. Geol.) Bull. 86, 1921–1938. https://doi.org/10.1306/61EEDDBE-173E-11D7-8645000102C1865D.
Curtis, M.E., Ambrose, R.J., Sondergeld, C.H., Rai, C.S., 2011. Investigation of the relationship between organic porosity and thermal maturity in the marcellus shale. In: SPE North American Uncoventional Gas Conference and Exhibition Held in the Woodlands, Texas, USA, 14-16 June. https://doi.org/10.2118/144370-MS. SPE Paper 144370.
Curtis, M.E., Ambrose, R.J., Sondergeld, C.H., 2010. Structural characterization of gas shales on the micro and nano scales. In: Canadian Unconventional Resources and International Petroleum Conference, Calgary, Alberta. https://doi.org/10.2118/137693-MS. October 19-21, SPE Paper 137693.
Curtis, M.E., Cardott, B.J., Sondergeld, C.H., Rai, C.S., 2012. Development of organic porosity in the Woodford Shale with increasing thermal maturity. Int. J. Coal Geol. 103, 26–31. https://doi.org/10.1016/j.coal.2012.08.004.
De Boer, P., Hoogenboom, J.P., Giepmans, B.N., 2015. Correlated light and electron microscopy: ultrastructure lights up. Nat. Methods 12, 503–513. https://doi.org/10.1038/nmeth.3400.
Dembicki Jr., H., 2009. Three common source rock evaluation errors made by geologists during prospect or play appraisals. AAPG (Am. Assoc. Pet. Geol.) Bull. 93, 341–356. https://doi.org/10.1306/10230808076.
Espitalie, J., Deroo, G., Marquis, F., 1985. Rock-Eval pyrolysis and its applications (part 2). Institut Français du Pétrole 40 (6), 755–784.
Everson, R.C., Neomagus, H.W., Kaitano, R., Falcon, R., van Alphen, C., du Cann, V.M., 2008. Properties of high ash char particles derived from inertinite-rich coal: 1. Chemical, structural and petrographic characteristics. Fuel 87, 3082–3090. https://doi.org/10.1016/j.fuel.2008.03.024.
Fishman, N.S., Hackley, P.C., Lowers, H.A., Hill, R.J., Egenhoff, S.O., Eberl, D.D., Blum, A.E., 2012. The nature of porosity in organic-rich mudstones of the upper jurassic Kimmeridge Clay Formation, north sea, offshore United Kingdom. Int. J. Coal Geol. 103, 32–50. https://doi.org/10.1016/j.coal.2012.07.012.
Fu, J.H., Li, S.X., Niu, X.B., Deng, X.Q., Zhou, X.P., 2020. Geological characteristics and exploration of shale oil in chang 7 member of triassic Yanchang Formation, Ordos Basin, NW China. Petrol. Explor. Dev. 47 (5), 931–945. https://doi.org/10.1016/S1876-3804(20)60107-0.
Gao, Z., Liang, Z., Hu, Q., Jiang, Z., Xuan, Q., 2021. A new and integrated imaging and compositional method to investigate the contributions of organic matter and inorganic minerals to the pore spaces of lacustrine shale in China. Mar. Petrol. Geol. 127, 104962. https://doi.org/10.1016/j.marpetgeo.2021.104962.
Giffin, S., Littke, R., Klaver, J., Urai, J.L., 2013. Application of BIB–SEM technology to characterize macropore morphology in coal. Int. J. Coal Geol. 114, 85–95. https://doi.org/10.1016/j.coal.2013.02.009.
Gou, Q., Xu, S., Hao, F., Yang, F., Zhang, B., Shu, Z., Gao, M., 2019. Full-scale pores and micro-fractures characterization using FE-SEM, gas adsorption, nano-CT and micro-CT: a case study of the Silurian Longmaxi Formation shale in the Fuling area, Sichuan Basin, China. Fuel 253, 167–179. https://doi.org/10.1016/j.fuel.2019.04.116.
Grobe, A., Schmatz, J., Littke, R., Klaver, J., Urai, J.L., 2017. Enhanced surface flatness of vitrinite particles by broad ion beam polishing and implications for reflectance measurements. Int. J. Coal Geol. 180, 113–121. https://doi.org/10.1016/j.coal.2017.05.006.
Guan, Q., Lü, X., Dong, D., Cai, X., 2019. Origin and significance of organic-matter pores in upper ordovician wufeng-lower silurian Longmaxi mudstones, sichuan basin. J. Petrol. Sci. Eng. 176, 554–561. https://doi.org/10.1016/j.petrol.2019.01.079.
Guo, H., He, R., Jia, W., Lei, Y., Luo, X., Wang, X., Jiang, C., 2018. Pore characteristics of lacustrine shale within the oil window in the upper triassic Yanchang Formation, southeastern Ordos Basin, China. Mar. Petrol. Geol. 91, 279–296. https://doi.org/10.1016/j.marpetgeo.2018.01.013.
Hackley, P.C., Valentine, B.J., Voortman, L.M., Hatcherian, J., 2017. Utilization of integrated correlative light and electron microscopy (iCLEM) for imaging sedimentary organic matter. J. Microsc. 267, 371–383. https://doi.org/10.1111/jmi.12576.
Han, H., Cao, Y., Chen, S.J., Lu, J.G., Huang, C.X., Zhu, H.H., Gao, Y., 2016b. Influence of particle size on gas-adsorption experiments of shales: an example from a Longmaxi Shale sample from the Sichuan Basin, China. Fuel 186, 750–757. https://doi.org/10.1016/j.fuel.2016.09.018.
Han, H., Pang, P., Li, Z.L., Shi, P.T., Guo, C., Liu, Y., Gao, Y., 2019. Controls of organic and inorganic compositions on pore structure of lacustrine shales of Chang 7 member from Triassic Yanchang Formation in the Ordos Basin, China. Mar. Petrol. Geol. 100, 270–284. https://doi.org/10.1016/j.marpetgeo.2018.10.038.
Han, H., Pang, P., Zhong, N., Luo, Q., Ma, Y., Gao, Y., 2020. The pore characteristics and gas potential of the Jurassic continental shales in the middlesmall basins, northwest China. J. Petrol. Sci. Eng. 188, 106873. https://doi.org/10.1016/j.petrol.2019.106873.
Han, H., Zhong, N., Ma, Y., Huang, C., Wang, Q., Chen, S., Lu, J., 2016a. Gas storage and controlling factors in an over-mature marine shale: a case study of the Lower Cambrian Lujiaping shale in the Dabashan arc-like thrust–fold belt, southwestern China. J. Nat. Gas Sci. Eng. 33, 839–853. https://doi.org/10.1016/j.jngse.2016.06.027.
Han, H., Liu, P.W., Ding, Z.G., Shi, P., Jia, J., Zhang, W., Gao, Y., 2018. The influence of extractable organic matter on pore development in the Late Triassic Chang 7 lacustrine shales, Yanchang Formation, Ordos Basin, China. Acta Geol. Sin. 92 (4), 1508–1522. https://doi.org/10.1111/1755-6724.13640.
Han, M.L., Wei, X.L., Zhang, J.C., Liu, Y., Tang, X., Li, P., Liu, Z.Y., 2022. Influence of structural damage on evaluation of microscopic pore structure in marine continental transitional shale of the Southern North China Basin: a method based on the low-temperature N2 adsorption experiment. Petrol. Sci. 19 (1), 100–115. https://doi.org/10.1016/j.petsci.2021.10.016.
Hartkopf-Fröder, C., Königshof, P., Littke, R., Schwarzbauer, J., 2015. Optical thermal maturity parameters and organic geochemical alteration at low grade diagenesis to anchimetamorphism: a review. Int. J. Coal Geol. 150, 74–119. https://

doi.org/10.1016/j.coal.2015.06.005.
Hu, G., Pang, Q., Jiao, K., Hu, C., Liao, Z., 2020. Development of organic pores in the Longmaxi Formation overmature shales: combined effects of thermal maturity and organic matter composition. Mar. Petrol. Geol. 116, 104314. https://doi.org/10.1016/j.marpetgeo.2020.104314.
Hu, H., Hao, F., Lin, J., Lu, Y., Ma, Y., Li, Q., 2017. Organic matter-hosted pore system in the Wufeng-Longmaxi (O3w-S11) shale, Jiaoshiba area, eastern Sichuan Basin, China. Int. J. Coal Geol. 173, 40–50. https://doi.org/10.1016/j.coal.2017.02.004.
Hu, T., Pang, X.Q., Jiang, F.J., Wang, Q.F., Wu, G.Y., Liu, X.H., Chen, Y.Y., 2021. Key factors controlling shale oil enrichment in saline lacustrine rift basin: implications from two shale oil wells in Dongpu Depression, Bohai Bay Basin. Petrol. Sci. 18 (3), 687–711. https://doi.org/10.1007/s12182-021-00564-z.
Jarvie, D.M., Claxton, B.L., Henk, F., Breyer, J.T., 2001. Oil and shale gas from the barnett shale, fort. Worth basin, Texas. AAPG Annual Meeting Program 10, A100.
Jarvie, D.M., Hill, R.J., Ruble, T.E., Pollastro, R.M., 2007. Unconventional shale-gas systems: the Mississippian Barnett Shale of north-central Texas as one model for thermogenic shale-gas assessment. AAPG (Am. Assoc. Pet. Geol.) Bull. 91, 475–499. https://doi.org/10.1306/12190606068.
Ji, W., Hao, F., Schulz, H., Song, Y., Tian, J., 2019. The architecture of organic matter and its pores in highly mature gas shales of the Lower Silurian Longmaxi Formation in the Upper Yangtze Platform, south China. AAPG (Am. Assoc. Pet. Geol.) Bull. 102 (12), 2909–2942. https://doi.org/10.1306/04101917386.
Ji, W., Song, Y., Rui, Z., Meng, M., Huang, H., 2017. Pore characterization of isolated organic matter from high matured gas shale reservoir. Int. J. Coal Geol. 174, 31–40. https://doi.org/10.1016/j.coal.2017.03.005.
Jia, Y., Han, D., Zhang, J., Wang, C., Lin, W., Ren, X., Chang, L., 2021. Differences in pore-forming efficiency among organic macerals and its restriction against reservoir quality: a case study based on the marine shale reservoir in the Longmaxi formation, southern sichuan basin, China. Lithosphere, 2700912. https://doi.org/10.2113/2021/2700912, 2021.
Jiang, F., Chen, D., Wang, Z., Xu, Z., Chen, J., Liu, L., Liu, Y., 2016. Pore characteristic analysis of a lacustrine shale: a case study in the Ordos Basin, NW China. Mar. Petrol. Geol. 73, 554–571. https://doi.org/10.1016/j.marpetgeo.2016.03.026.
Jing, Z., Gao, S., Rodrigues, S., Underschultz, J., Strounina, E., Pan, S., Steel, K.M., 2021. Influence of porosity on the reactivity of inertinite and vitrinite toward sodium hypochlorite: implications for enhancing coal seam gas development. Int. J. Coal Geol. 237, 103709. https://doi.org/10.1016/j.coal.2021.103709.
Khorasani, G.K., Michelsen, J.K., 1991. Geological and laboratory evidence for early generation of large amounts of liquid hydrocarbons from suberinite and subereous components. Org. Geochem. 17, 849–863. https://doi.org/10.1016/0146-6380(91)90025-F.
Klaver, J., Desbois, G., Littke, R., Urai, J.L., 2016. BIB-SEM pore characterization of mature and post mature Posidonia Shale samples from the Hils area, Germany. Int. J. Coal Geol. 158, 78–89. https://doi.org/10.1016/j.coal.2016.03.003.
Kuang, L.C., Hou, L.H., Wu, S.T., Cui, J.W., Tian, H., Zhang, L.J., Jiang, X.H., 2022. Organic matter occurrence and pore-forming mechanisms in lacustrine shales in China. Petrol. Sci. 19 (4), 1460–1472. https://doi.org/10.1016/j.petsci.2022.03.005.
Lei, Y., Luo, X., Wang, X., Zhang, L., Jiang, C., Yang, W., Zhang, L., 2015. Characteristics of silty laminae in Zhangjiatan Shale of southeastern Ordos Basin, China: implications for shale gas formation. AAPG (Am. Assoc. Pet. Geol.) Bull. 99, 661–687. https://doi.org/10.1306/09301414059.
Lin, Y., Qin, Y., Ma, D., Duan, Z., 2021. Pore structure, adsorptivity and influencing factors of high-volatile bituminous coal rich in inertinite. Fuel 293, 120418. https://doi.org/10.1016/j.fuel.2021.120418.
Liu, B., Schieber, J., Mastalerz, M., 2017. Combined SEM and reflected light petrography of organic matter in the New Albany Shale (Devonian-Mississippian) in the Illinois Basin: a perspective on organic pore development with thermal maturation. Int. J. Coal Geol. 184, 57–72. https://doi.org/10.1016/j.coal.2017.11.002.
Liu, B., Mastalerz, M., Schieber, J., 2022. SEM petrography of dispersed organic matter in black shales: a review. Earth Sci. Rev. 224, 103874. https://doi.org/10.1016/j.earscirev.2021.103874.
Liu, K., Wang, L., Ostadhassan, M., Zou, J., Bubach, B., Rezaee, R., 2019. Nanopore structure comparison between shale oil and shale gas: examples from the Bakken and Longmaxi Formations. Petrol. Sci. 16 (1), 77–93. https://doi.org/10.1007/s12182-018-0277-3.
Liu, X.P., Guan, M., Jin, Z.J., Cao, Z., Lai, J., Zheng, L.J., Chen, S.Y., 2022. Pore structure evolution of lacustrine organic-rich shale from the second member of the Kongdian formation in the Cangdong Sag, Bohai Bay Basin, China. Petrol. Sci. 19 (2), 459–471. https://doi.org/10.1016/j.petsci.2021.12.010.
Loucks, R.G., Reed, R.M., Ruppel, S.C., Hammes, U., 2012. Spectrum of pore types and networks in mudrocks and a descriptive classification for matrix-related mudrock pores. AAPG (Am. Assoc. Pet. Geol.) Bull. 96, 1071–1098. https://doi.org/10.1306/08171111061.
Löhr, S.C., Baruch, E.T., Hall, P.A., Kennedy, M.J., 2015. Is organic pore development in gas shales influenced by the primary porosity and structure of thermally immature organic matter? Org. Geochem. 87, 119–132. https://doi.org/10.1016/j.orggeochem.2015.07.010.
Loucks, R.G., Reed, R.M., 2014. Scanning-electron-microscope petrographic evidence for distinguishing organic-matter pores associated with depositional organic matter versus migrated organic matter in mudrock. GCAGS Journal 3, 51–60.
Loucks, R.G., Reed, R.M., Ruppel, S.C., Jarvie, D.M., 2009. Morphology, genesis, and distribution of nanometer-scale pores in siliceous mudstones of the Mississippian barnett shale. J. Sediment. Res. 79 (12), 848–861. https://doi.org/10.2110/jsr.2009.092.
Luo, Q., Zhong, N., Dai, N., Zhang, W., 2016. Graptolite-derived organic matter in the wufeng–longmaxi formations (upper ordovician–lower silurian) of southeastern chongqing, China: implications for gas shale evaluation. Int. J. Coal Geol. 153, 87–98. https://doi.org/10.1016/j.coal.2015.11.014.
Ma, Y., Ardakani, O.H., Zhong, N., Liu, H., Huang, H., Larter, S., Zhang, C., 2020. Possible pore structure deformation effects on the shale gas enrichment: an example from the Lower Cambrian shales of the Eastern Upper Yangtze Platform, South China. Int. J. Coal Geol. 217, 103349. https://doi.org/10.1016/j.coal.2019.103349.
Ma, Y., Zhong, N., Cheng, L., Pan, Z., Dai, N., Zhang, Y., Yang, L., 2016. Pore structure of the graptolite-derived OM in the Longmaxi shale, southeastern upper yangtze region, China. Mar. Petrol. Geol. 72, 1–11. https://doi.org/10.1016/j.marpetgeo.2016.01.009.
Ma, Y., Zhong, N.N., Li, D.H., Pan, Z., Cheng, L., Liu, K., 2015. Organic matter/clay mineral intergranular pores in the Lower Cambrian Lujiaping shale in the northeastern part of the upper Yangtze area, China: a possible microscopic mechanism for gas preservation. Int. J. Coal Geol. 137, 38–54. https://doi.org/10.1016/j.coal.2014.11.001.
Mastalerz, M., Schieber, J., 2017. Effect of ion milling on the perceived maturity of shale samples: implications for organic petrography and SEM analysis. Int. J. Coal Geol. 183, 110–119. https://doi.org/10.1016/j.coal.2017.10.010.
Mastalerz, M., Schimmelmann, A., Drobniak, A., Chen, Y., 2013. Porosity of Devonian and Mississippian New Albany Shale across a maturation gradient: insights from organic petrology, gas adsorption, and mercury intrusion. AAPG (Am. Assoc. Pet. Geol.) Bull. 97, 1621–1643. https://doi.org/10.1306/04011312194.
Milliken, K.L., Rudnicki, M., Awwiller, D.N., Zhang, T., 2013. Organic matterehosted pore system, Marcellus formation (Devonian), Pennsylvania. AAPG (Am. Assoc. Pet. Geol.) Bull. 97 (2), 177–200. https://doi.org/10.1306/07231212048.
Misch, D., Gross, D., Hawranek, G., Horsfield, B., Klaver, J., Mendez-Martin, F., Zou, C., 2019. Solid bitumen in shales: petrographic characteristics and implications for reservoir characterization. Int. J. Coal Geol. 205, 14–31. https://doi.org/10.1016/j.coal.2019.02.012.
Modica, C.J., Lapierre, S.G., 2012. Estimation of kerogen porosity in source rocks as a function of thermal transformation: example from the Mowry Shale in the Powder River Basin of Wyoming. AAPG (Am. Assoc. Pet. Geol.) Bull. 96, 87–108. https://doi.org/10.1306/04111110201.
Pacton, M., Fiet, N., Gorin, G., 2006. Revisiting amorphous organic matter in Kimmeridgian laminites: what is the role of the vulcanization process in the amorphization of organic matter? Terra. Nova 18, 380–387. https://doi.org/10.1111/j.1365-3121.2006.00702.x.
Pang, P., Han, H., Hu, L., Guo, C., Gao, Y., Xie, Y., 2021. The calculations of pore structure parameters from gas adsorption experiments of shales: which models are better? J. Nat. Gas Sci. Eng., 104060 https://doi.org/10.1016/j.jngse.2021.104060.
Pang, Q., Hu, G., Jiao, K., Tan, X., Liu, H., Ye, Y., Zhao, D., 2018. Characteristics of organic pores and composition of bio-precursors in the Wufeng and Longmaxi formation shales, southern sichuan basin, China. Energy Explor. Exploit. 36, 645–664. https://doi.org/10.1177/0144598717753166.
Peters, K.E., Walters, C.C., Moldowan, J.M., 2005. The Biaomaker Guide. Biomarkers and Isotopes in the Environment and Human History, second ed., vol. 1. Cambridge University Press, New York, p. 471p.
Piane, C.D., Bourdet, J., Josh, M., Clennell, M.B., Rickard, W.D., Saunders, M., Raven, M.D., 2018. Organic matter network in post-mature Marcellus Shale: effects on petrophysical properties. AAPG (Am. Assoc. Pet. Geol.) Bull. 102, 2305–2332. https://doi.org/10.1306/04121817180.
Polishchuk, R.S., Polishchuk, E.V., Marra, P., Alberti, S., Buccione, R., Luini, A., Mironov, A.A., 2000. Correlative light-electron microscopy reveals the tubular-saccular ultrastructure of carriers operating between Golgi apparatus and plasma membrane. JCB (J. Cell Biol.) 148, 45–58. https://doi.org/10.1083/jcb.148.1.45.
Pommer, M., Milliken, K., 2015. Pore types and pore-size distributions across thermal maturity, Eagle Ford Formation, southern Texas. AAPG (Am. Assoc. Pet. Geol.) Bull. 99, 1713–1744. https://doi.org/10.1306/03051514151.
Qiao, J., Baniasad, A., Zieger, L., Zhang, C., Luo, Q., Littke, R., 2021. Paleo-depositional environment, origin and characteristics of organic matter of the triassic chang 7 member of the Yanchang Formation throughout the mid-western part of the Ordos Basin, China. Int. J. Coal Geol. 237, 103636. https://doi.org/10.1016/j.coal.2020.103636.
Rexer, T.F., Mathia, E.J., Aplin, A.C., Thomas, K.M., 2014. High-pressure methane adsorption and characterization of pores in Posidonia shales and isolated kerogens. Energy & Fules 28, 2886–2901. https://doi.org/10.1021/ef402466m.
Romero-Sarmiento, M.-F., Ducros, M., Carpentier, B., Lorant, F., Cacas, M.C., Pegaz-Fiornet, S., Moretti, I., 2013. Quantitative evaluation of TOC, organic porosity and gas retention distribution in a gas shale play using petroleum system modeling: application to the Mississippian Barnett Shale. Mar. Petrol. Geol. 45, 315–330.

https://doi.org/10.1016/j.marpetgeo.2013.04.003.
Ross, D.J., Bustin, R.M., 2009. The importance of shale composition and pore structure upon gas storage potential of shale gas reservoirs. Mar. Petrol. Geol. 26, 916–927. https://doi.org/10.1016/j.marpetgeo.2008.06.004.
Sanei, H., Ardakani, O.H., 2016. Alteration of organic matter by ion milling. Int. J. Coal Geol. 163, 123–131. https://doi.org/10.1016/j.coal.2016.06.021.
Sanei, H., Haeri-Ardakani, O., Wood, J.M., Curtis, M.E., 2015. Effects of nanoporosity and surface imperfections on solid bitumen reflectance (BRo) measurements in unconventional reservoirs. Int. J. Coal Geol. 138, 95–102. https://doi.org/10.1016/j.coal.2014.12.011.
Schieber, J., 2013. SEM observations on ion-milled samples of Devonian Black Shales from Indiana and New York: the petrographic context of multiple pore types. In: Camp, W., Diaz, E., Wawak, B. (Eds.), Electron Microscopy of Shale Hydrocarbon Reservoirs: AAPG Memoir 102, 153–171.
Shan, C., Zhang, T., Liang, X., Zhang, Z., Wang, M., Zhang, K., Zhu, H., 2018. On the fundamental difference of adsorption-pores systems between vitrinite- and inertinite-rich anthracite derived from the southern Sichuan basin, China. J. Nat. Gas Sci. Eng. 53, 32–44. https://doi.org/10.1016/j.jngse.2018.02.025.
Sing, K., 2001. The use of nitrogen adsorption for the characterisation of porous materials. Colloids Surf. A Physicochem. Eng. Asp. 187, 3–9. https://doi.org/10.1016/S0927-7757(01)00612-4.
Sing, K.S.W., Everett, D.H., Haul, R.A.W., 1985. Reporting physisorption data for gas/solid systems with special reference to the determination of surface area and porosity (Recommendations 1984). Pure Appl. Chem. 57 (4), 603–619. https://doi.org/10.1351/pac198557040603.
Sisk, C., Diaz, D., Walls, A., Grader, A., Suhrer, M., 2010. 3D visualization and classifcation of pore structure and pore flling in gas shales. In: SPE Annual Technical Conference and Exhibition, Florence, Italy. https://doi.org/10.2118/134582-MS. September 19-22, SPE Paper 134582.
Slatt, R.M., O'Brien, N.R., 2011. Pore types in the Barnett and Woodford gas shales: contribution to understanding gas storage and migration pathways in fne-grained rocks. AAPG (Am. Assoc. Pet. Geol.) Bull. 95 (12), 2017–2030. https://doi.org/10.1306/03301110145.
Snowdon, L.R., Powell, T., 1982. Immature oil and condensate—modification of hydrocarbon generation model for terrestrial organic matter. AAPG (Am. Assoc. Pet. Geol.) Bull. 66, 775–788. https://doi.org/10.1306/03B5A313-16D1-11D7-8645000102C1865D.
Sondergeld, C.H., Newsham, K.E., Comisky, J.T., Rice, M.C., Rai, C.S., 2010. Petrophysical considerations in evaluating and producing shale gas resources. In: Society of Petroleum Engineers Unconventional Gas Conference, Pittsburgh, USA. https://doi.org/10.2118/131768-MS. February 23-25, SPE Paper 131768.
Stach, E., Machowsky, M.T., Teichmueller, M., 1982. Stach's Texbook of Coal Petrology, third ed., p. 569p Stuttgart, E.
Strąpoć, D., Mastalerz, M., Schimmelmann, A., Drobniak, A., Hasenmueller, N.R., 2010. Geochemical constraints on the origin and volume of gas in the new Albany shale (Devonian-Mississippian), eastern Illinois basin. AAPG (Am. Assoc. Pet. Geol.) Bull. 94 (11), 1713–1740. https://doi.org/10.1306/06301009197.
Suárez-Ruiz, I., Flores, D., Mendonca Filho, J.G., Hackley, P.C., 2012. Review and update of the applications of organic petrology: Part 1, geological applications. Int. J. Coal Geol. 99, 54–112. https://doi.org/10.1016/j.coal.2012.02.004.
Sun, L., Tuo, J., Zhang, M., Wu, C., Wang, Z., Zheng, Y., 2015. Formation and development of the pore structure in Chang 7 member oil-shale from Ordos Basin during organic matter evolution induced by hydrous pyrolysis. Fuel 158, 549–557. https://doi.org/10.1016/j.fuel.2015.05.061.
Synnott, D.P., Sanei, H., Pedersen, P.K., Dewing, K., Ardakani, O.H., 2016. The effect of bacterial degradation on bituminite reflectance. Int. J. Coal Geol. 162, 34–38. https://doi.org/10.1016/j.coal.2016.05.016.
Taylor, G.H., Teichmüller, M., Davis, A., Diessel, C.F.K., Littke, R., Robert, P., 1998. Organic Petrology. Gebrüder Borntraeger, Berlin, p. 704p.
Teng, J., Mastalerz, M., Hampton, L., 2017. Maceral controls on porosity characteristics of lithotypes of Pennsylvanian high volatile bituminous coal: example from the Illinois Basin. Int. J. Coal Geol. 172, 80–94. https://doi.org/10.1016/j.coal.2017.02.001.
Tian, H., Pan, L., Xiao, X., Wilkins, R.W., Meng, Z., Huang, B., 2013. A preliminary study on the pore characterization of Lower Silurian black shales in the Chuandong Thrust Fold Belt, southwestern China using low pressure N2 adsorption and FE-SEM methods. Mar. Petrol. Geol. 48, 8–19. https://doi.org/10.1016/j.marpetgeo.2013.07.008.
Tian, H., Pan, L., Zhang, T., Xiao, X., Meng, Z., Huang, B., 2015. Pore characterization of organic-rich lower Cambrian shales in Qiannan depression of Guizhou province, Southwestern China. Mar. Petrol. Geol. 62, 28–43. https://doi.org/10.1016/j.marpetgeo.2015.01.004.
Timmermans, F.J., Otto, C., 2015. Contributed review: review of integrated correlative light and electron microscopy. Rev. Sci. Instrum. 86, 011501. https://doi.org/10.1063/1.4905434.
Tissot, B.P., Welte, D.H., 1978. Petroleum Formation and Occurrence. Springer–Verlag.
Unsworth, J.F., Fowler, C.S., Jones, L.F., 1989. Moisture in coal: 2. Maceral effects on pore structure. Fuel 68, 18–26. https://doi.org/10.1016/0016-2361(89)90005-7.
Valentine, B.J., Hackley, P.C., Hatcherian, J., Yu, J.J., 2019. Reflectance increase from broad beam ion milling of coals and organic-rich shales due to increased surface flatness. Int. J. Coal Geol. 201, 86–101. https://doi.org/10.1016/j.coal.2018.11.004.
Vranjes-Wessely, S., Misch, D., Issa, I., Kiener, D., Fink, R., Seemann, T., Sachsenhofer, R.F., 2020. Nanoscale pore structure of Carboniferous coals from the Ukrainian Donets Basin: a combined HRTEM and gas sorption study. Int. J. Coal Geol. 224, 103484. https://doi.org/10.1016/j.coal.2020.103484.
Wang, P., Jiang, Z., Yin, L., Chen, L., Li, Z., Zhang, C., Huang, P., 2017. Lithofacies classification and its effect on pore structure of the Cambrian marine shale in the Upper Yangtze Platform, South China: evidence from FE-SEM and gas adsorption analysis. J. Petrol. Sci. Eng. 156, 307–321. https://doi.org/10.1016/j.petrol.2017.06.011.
Wang, P., Zhang, C., Li, X., Zhang, K., Yuan, Y., Zang, X., Jiang, Z., 2020. Organic matter pores structure and evolution in shales based on the he ion microscopy (HIM): a case study from the Triassic Yanchang, Lower Silurian Longmaxi and Lower Cambrian Niutitang shales in China. J. Nat. Gas Sci. Eng. 84, 103682. https://doi.org/10.1016/j.jngse.2020.103682.
Wang, M., Sherwood, N., Li, Z.S., Lu, S., Wang, W., Huang, A., Lu, K., 2015a. Shale oil occurring between salt intervals in the Dongpu Depression, Bohai Bay basin, China. Int. J. Coal Geol. 152, 100–112. https://doi.org/10.1016/j.coal.2015.07.004.
Wang, M., Wilkins, R.W.T., Song, G.Q., Zhang, L., Xu, X., Li, Z., Chen, G., 2015b. Geochemical and geological characteristics of the Es3L lacustrine shale in the Bonan sag, Bohai Bay basin, China. Int. J. Coal Geol. 138, 16–29. https://doi.org/10.1016/j.coal.2014.12.007.
Wang, T.Y., Tian, S.C., Liu, Q.L., Li, G.S., Sheng, M., Ren, W.X., Zhang, P.P., 2021. Pore structure characterization and its effect on methane adsorption in shale kerogen. Petrol. Sci. 18 (2), 565–578. https://doi.org/10.1007/s12182-020-00528-9.
Wang, X.Q., Zhai, Z.Q., Jin, X., Wu, S.T., Li, J.M., Sun, L., Liu, X.D., 2016. Molecular simulation of CO2/CH4 competitive adsorption in organic matter pores in shale under certain geological conditions. Petrol. Explor. Dev. 43 (5), 841–848. https://doi.org/10.1016/S1876-3804(16)30100-8.
Wang, Y., Wang, L., Wang, J., Jiang, Z., Jin, C., Wang, Y., 2018. Characterization of organic matter pores in typical marine and terrestrial shales, China. J. Nat. Gas Sci. Eng. 49, 56–65. https://doi.org/10.1016/j.jngse.2017.11.002.
Wei, M.M., Zhang, L., Xiong, Y.Q., Li, J., 2016. Nanopore structure characterization for organic-rich shale using the non-local-density functional theory by a combination of N2 and CO2 adsorption. Microporous Mesoporous Mater. 227, 88–94. https://doi.org/10.1016/j.micromeso.2016.02.050.
Xiao, X.M., Zhao, B.Q., Thu, Z.L., Song, Z.G., Wilkins, R.W.T., 2005. Upper paleozoic petroleum system, Ordos Basin, China. Mar. Petrol. Geol. 22 (8), 945–963. https://doi.org/10.1016/j.marpetgeo.2005.04.001.
Yang, C., Xiong, Y., Zhang, J., Liu, Y., Chen, C., 2019. Comprehensive understanding of OM-hosted pores in transitional shale: a case study of permian longtan shale in south China based on organic petrographic analysis, gas adsorption, and X-ray diffraction measurements. Energy & Fules. 33, 8055–8064. https://doi.org/10.1021/acs.energyfuels.9b01410.
Yang, C., Zhang, J., Han, S., Xue, B., Zhao, Q., 2016a. Classification and the developmental regularity of organic-associated pores (OAP) through a comparative study of marine, transitional, and terrestrial shales in China. J. Nat. Gas Sci. Eng. 36, 358–368. https://doi.org/10.1016/j.jngse.2016.10.044.
Yang, C., Zhang, J., Wang, X., Tang, X., Chen, Y., Jiang, L., Gong, X., 2017. Nanoscale pore structure and fractal characteristics of a marine-continental transitional shale: a case study from the lower Permian Shanxi Shale in the southeastern Ordos Basin, China. Mar. Petrol. Geol. 88, 54–68. https://doi.org/10.1016/j.marpetgeo.2017.07.021.
Yang, F., Ning, Z., Liu, H., 2014. Fractal characteristics of shales from a shale gas reservoir in the Sichuan Basin, China. Fuel 115, 378–384. https://doi.org/10.1016/j.fuel.2013.07.040.
Yang, H., Li, S., Liu, X., 2013. Characteristics and resource prospects of tight oil and shale oil in Ordos Basin. Acta Pet. Sin. 34, 1–11. https://doi.org/10.7623/syxb201301001.
Yang, R., He, S., Yi, J., Hu, Q., 2016b. Nano-scale pore structure and fractal dimension of organic-rich Wufeng-Longmaxi shale from Jiaoshiba area, Sichuan Basin: investigations using FE-SEM, gas adsorption and helium pycnometry. Mar. Petrol. Geol. 70, 27–45. https://doi.org/10.1016/j.marpetgeo.2015.11.019.
Yao, L., Zhong, N., Khan, I., Chen, J., Luo, Q., Zhang, Y., Sun, W., 2021. Comparison of in-source solid bitumen with migrated solid bitumen from Ediacaran-Cambrian rocks in the Upper Yangtze region, China. Int. J. Coal Geol. 240, 103748. https://doi.org/10.1016/j.coal.2021.103748.
Zhang, J., Tang, Y., He, D., Sun, P., Zou, X., 2020b. Full-scale nanopore system and fractal characteristics of clay-rich lacustrine shale combining FE-SEM, nano-CT, gas adsorption and mercury intrusion porosimetry. Appl. Clay Sci. 196, 105758. https://doi.org/10.1016/j.clay.2020.105758.
Zhang, W., Hu, W., Borjigin, T., Zhu, F., 2020a. Pore characteristics of different organic matter in black shale: a case study of the Wufeng-Longmaxi Formation

in the Southeast Sichuan Basin, China. Mar. Petrol. Geol. 111, 33–43. https://doi.org/10.1016/j.marpetgeo.2019.08.010.
Zhao, Y., Liu, S., Elsworth, D., Jiang, Y., Zhu, J., 2014. Pore structure characterization of coal by synchrotron small-angle X-ray scattering and transmission electron microscopy. Energy & Fules 28, 3704–3711. https://doi.org/10.1021/ef500487d.
Zhou, S., Liu, D., Cai, Y., Karpyn, Z., Yao, Y., 2018. Comparative analysis of nanopore structure and its effect on methane adsorption capacity of Southern Junggar coalfield coals by gas adsorption and FIB-SEM tomography. Microporous Mesoporous Mater. 272, 117–128. https://doi.org/10.1016/j.micromeso.2018.06.027.